Applied Ocean Research 59 (2016) 93–114

Contents lists available at ScienceDirect

Applied Ocean Research

journal homepage: www.elsevier.com/locate/apor

A new time domain Rankine panel method for simulations involving multiple bodies with large relative displacements

R.A. Watai*, F. Ruggeri, A.N. Simos

Numerical Offshore Tank (TPN), Department of Naval Architecture and Ocean Engineering – University of Sao Paulo, Sao Paulo, SP, Brazil

ARTICLE INFO

Article history:
Received 11 August 2015
Received in revised form 29 January 2016
Accepted 9 May 2016
Available online 9 June 2016

Keywords:
Time domain Rankine panel method
Large relative motions
Multibody hydrodynamic interaction

ABSTRACT

Many important offshore operations involve multiple vessels whose relative positions change considerably in the course of the operational procedures. When the action of sea waves on the dynamics of these vessels is concerned, an accurate modeling of the hydrodynamic problem is not an easy task. The use of frequency-domain panel codes is compromised by the variations of the bodies' relative positions and may lead to inconsistent results. A time-domain approach is clearly more appropriate, but even in this case the representation of the moving bodies requires a re-meshing procedure and considerable computational efforts. This paper addresses the problem of wave interaction with multiple bodies with large relative displacement by integrating a re-meshing procedure to a time-domain Rankine panel code. The mathematical algorithms adopted for generating the new free-surface grids and performing the interpolation of wave elevation and velocity potential are described in detail. The paper also presents a set of dedicated captive model tests performed in a wave basin as a means of verifying the performance of the numerical method. Tests involved models with simple geometries that performed slow prescribed drift motions in the presence of incoming regular waves. Hydrodynamic forces were measured on one of the models and different levels of transient interaction effects could be reached by varying the frequency ratios between waves and body motions. The good performance of the method is then attested by directly comparing the hydrodynamic forces predicted by the computational code with those measured during the model tests. Moreover, it will be shown that the numerical model was able to capture some interesting Doppler effects that will be discussed together with other validation results.

1. Introduction

The Numerical Offshore Tank (Tanque de Provas Numérico – TPN – see for instance Nishimoto et al. [1]) is a research center dedicated to the simulation of offshore operations. Opened in 2001, most of its works focus on the development of numerical models in topics such as wave-structure interaction, sloshing, flow-induced motions and vibrations and the dynamics of mooring lines and risers. All these numerical models are then combined and linked to assess the seakeeping performance of offshore systems and marine operations by means of a range of time-domain simulators.

In this context, modeling wave-induced forces and body responses in time domain is a critical topic that has always gained much attention, especially when the purpose is to deal with operations that involve multiple bodies and large relative displacements. Many practical operations require an update of the hydrodynamic interaction effects between different vessels in the time-span of a simulation. Examples are tandem offloading operations in which the direction of wind, waves or current is suddenly changing, or when the shuttle is moving due to fishtailing, floatover operations when a barge with topsides is docking between the columns of a semisubmersible unit, and the berthing manoeuver of ships in offshore terminals.

In TPN, a first attempt to improve the analysis of offloading operations of an FPSO platform in tandem configuration was made in 2004 by coupling a frequency-domain radiation-diffraction code to the TPN time-domain simulator. The objective was to recompute the hydrodynamic coefficients according to variations in the relative position of the vessels, as reported by Tannuri et al. [2]. Obviously, this approach is not free of problems and the main difficulties arise from discontinuities in the time history of the hydrodynamic forces, which in their turn are directly linked to the time-step considered when accounting for the changes in the positions of the vessels. Despite the computational hazard, however, by using this approach the authors were able to demonstrate that significant errors in the prediction of the shuttle tanker offset

* Corresponding author.
E-mail address: rafael.watai@usp.br (R.A. Watai).

http://dx.doi.org/10.1016/j.apor.2016.05.002
0141-1187/

and first-order motions would occur in many situations in case the hydrodynamic update is not performed. The analysis of this kind of operation was later extended by Queiroz Filho and Tannuri [3] for considering the use of DP shuttle tankers. Again, simulations have shown that a hydrodynamic update led to considerable differences in the results, both in terms of the power required by the DP system to maintain the vessel position and with respect to the trajectories followed by the shuttle tanker in case of a DP failure.

More recently, Bunnik [4] used a similar approach for dealing with the berthing manoeuver of an LNG carrier supported by tugboats and showed that, depending on the wave direction, the changes in the hydrodynamic interaction effects may have a considerable impact in the time required to complete the operation.

Both Tannuri et al. [2] and Bunnik [4] correctly remind that treating the hydrodynamic solutions in a quasi-static manner leads to inconsistencies for the fact that memory effects would now comprise velocities that are related to a different position in the past. Moreover, Tannuri et al. [2] also emphasizes problems in the history of hydrodynamic forces since spurious impulsive effects are introduced in the simulations.

In this paper a different approach is adopted, one that copes with the hydrodynamics of multiple bodies with large relative displacements in time-domain. This is done by means of a time-domain Rankine panel method (TDRPM) that is currently under development in TPN. The version of the code that is employed here only deals with linear wave-induced effects and the discretization is based on a low-order scheme. Information on the basis-version of TDRPM code can be found in Watai [5] and Watai et al. [6]. For dealing with the multi-body problem, a re-meshing procedure was implemented based on a generator of unstructured grids that was integrated to the time-loop of the TDRPM code and also on an interpolation algorithm used to compute the wave elevation and velocity potential on the new free-surface points.

A set of dedicated experiments involving captive model-tests was then conducted at TPN wave basin for the sake of verification of the numerical procedure. Tests involved two surface-piercing circular cylinders with slow prescribed horizontal motions in regular waves and the measurement of hydrodynamic forces. By changing the frequency of the prescribed oscillatory motions in respect to the incoming wave frequency, different levels of transient effects in the interaction forces could be achieved. Time histories of the forces were then adopted as benchmark and compared to those predicted in the time-domain simulations of TDRPM. As the results presented ahead will confirm, a very good agreement was reached in all cases.

The present article aims at describing the computational methods adopted for the re-meshing procedure and the verification of the code performance based on the captive model tests. For this, it is organized as follows: In Section 2, the TDRPM is presented, giving emphasis to the boundary value problem, numerical method and also the algorithm that performs the re-meshing of the free surface grid and the interpolation schemes used for the determination of the quantities at the new points of the surface. Section 3 brings a detailed description of the model tests conducted at the TPN wave basin, the main characteristics of the numerical models applied on the simulations and also the verification of the computation code, which comprises the comparisons between numerical and experimental results. Finally, conclusions are addressed in Section 4.

2. Time domain Rankine panel method (TDRPM)

The present version of the code is written in MATLAB environment and the solution of the seakeeping problem boundary value problem (BVP) is based on a three-dimensional low order panel method using the Rankine source as Green's function.

The mathematical description of the physical problem here addressed considers the same situation tested in the wave basin (described in Section 3.1), which comprises two cylinder bodies with one of them fixed and the other undergoing large and prescribed horizonal displacements. Moreover, the system is subjected to the action of incoming gravity waves assumed to be propagating in infinity depth.

2.1. Boundary value problem

The boundary value problem is formulated with respect to an earth-fixed coordinate system. The flow is assumed irrotational and incompressible whereas the fluid is assumed inviscid and homogeneous, allowing the problem to be solved under the hypothesis of the potential flow theory, in which the velocity field is defined by the gradient of a scalar field or velocity potential Φ.

The incident wave and the resultant body motions are here assumed to be of small amplitude. In addition, the problem is linearized by expanding the velocity potential and other physical quantities in power series and by applying the boundary conditions with respect to the mean surface positions.

By following this approach, the total velocity potential Φ is split in a sum of the incident wave velocity potential ϕ_I and the disturbed velocity potential $\phi^{(1)}$, the latter representing the disturbance of the incident waves diffracted from the bodies.

The incident regular wave field potential for infinite waters is defined as follows:

$$\phi_I^{(1)} = \frac{A_I g}{\omega} e^{kz} \cos(kx - \omega t) \quad \text{on} \quad z \leq 0, \tag{1}$$

where g, A_I, ω and k are the gravity acceleration, the incident wave amplitude, the wave angular frequency and the wave number, respectively.

Upon these considerations, the well known first order boundary value problem may be summarized as follows:

1. Laplace's equation:

$$\nabla^2 \phi = 0 \quad \text{in fluid domain.} \tag{2}$$

2. Kinematic free surface condition:

$$\frac{\partial \phi^{(1)}}{\partial z} = -\frac{\partial \eta^{(1)}}{\partial t} \quad \text{on} \quad z = 0. \tag{3}$$

3. Dynamic free surface condition:

$$\eta^{(1)} = -\frac{1}{g}\frac{\partial \phi^{(1)}}{\partial t} = 0 \quad \text{on} \quad z = 0. \tag{4}$$

4. Bodies' boundary conditions:

$$\nabla \phi^{(1)} \cdot \overline{\overline{n}}_{b1} = -\nabla \phi_I \cdot \overline{\overline{n}}_{b1} \quad \text{on} \quad \overline{S}_{b1}. \tag{5}$$

$$\nabla \phi^{(1)} \cdot \overline{\overline{n}}_{b2} = -\nabla \phi_I \cdot \overline{\overline{n}}_{b2} + \dot{\overline{x}}_2 \cdot \overline{\overline{n}}_{b2} \quad \text{on} \quad \overline{S}_{b2}(t). \tag{6}$$

5. Far field radiation condition:

$$\nabla \phi^{(1)} \to 0 \quad \text{at} \quad \sqrt{x^2 + y^2 + z^2} \to \infty \tag{7}$$

where $\eta^{(1)}$ is the first order free surface elevation; $\overline{\overline{n}}_{b1}$ and $\overline{\overline{n}}_{b2}$ are the zeroth order normal unit vectors of the bodies; $\overline{S}_{b1}$ and $\overline{S}_{b2}$ are the mean wetted surfaces of the bodies, and $\dot{\overline{x}}_2$ is the prescribed velocity vector of Body 2, respectively.

In order to conclude this initial boundary value problem (IBVP), an initial condition must be imposed at the free surface so as to determine the subsequent fluid motions. As demonstrated by Stoker [7], for flows beginning from rest we may set the velocity potential at the initial instant $t = 0$ s, to:

$$\Phi = 0 \quad \text{on} \quad t = 0\,\text{s} \tag{8}$$

The first order unsteady hydrodynamic pressure, forces and moments on the body hulls are calculated with Eqs. (9), (10) and (11), respectively:

$$p^{(1)} = -\rho\left(\frac{\partial\phi^{(1)}}{\partial t} + \frac{\partial\phi_I}{\partial t}\right), \tag{9}$$

$$\vec{F}^{(1)} = \iint_{\bar{S}_B} -\rho\left(\frac{\partial\phi^{(1)}}{\partial t} + \frac{\partial\phi_I}{\partial t}\right)\bar{\bar{n}}\,\mathrm{d}S, \tag{10}$$

$$\vec{M}_O^{(1)} = \iint_{\bar{S}_B} -\rho\left(\frac{\partial\phi^{(1)}}{\partial t} + \frac{\partial\phi_I}{\partial t}\right)(\bar{\bar{r}}\times\bar{\bar{n}})\,\mathrm{d}S. \tag{11}$$

One should notice that special care must be given to the linear pressure calculation, since there is not an exact equation for the calculation of the potential time-derivative $\partial\phi^{(1)}/\partial t$. In this way, we applied the numerical procedures demonstrated in van Daalen [8] and Tanizawa [9], in which the pressure is evaluated directly using the first order acceleration potential (12), which also satisfies Laplace's equation in the fluid domain:

$$\Psi^{(1)} = \frac{\partial\phi^{(1)}}{\partial t}. \tag{12}$$

By following this method, a second boundary value problem is written for the acceleration potential. The bodies boundary conditions can be defined by derivation in time of the expressions (5) and (6), as can be seen in (13) and (14).

$$\nabla\Psi^{(1)}\cdot\bar{\bar{n}}_{b1} = -\nabla\left(\frac{\partial\phi_I}{\partial t}\right)\cdot\bar{\bar{n}}_{b1} \quad \text{on} \quad \bar{S}_{b1}. \tag{13}$$

$$\nabla\Psi^{(1)}\cdot\bar{\bar{n}}_{b2} = -\nabla\left(\frac{\partial\phi_I}{\partial t}\right)\cdot\bar{\bar{n}}_{b2} + \ddot{\bar{x}}_2\cdot\bar{\bar{n}}_{b2} \quad \text{on} \quad \bar{S}_{b2}(t). \tag{14}$$

where $\ddot{\bar{x}}_2$ is the prescribed acceleration of Body 2.

In addition, the free surface boundary condition is determined in terms of the dynamic free surface condition for the velocity potential, as presented in (15):

$$\Psi^{(1)} = -g\eta^{(1)} \quad \text{on} \quad z = 0. \tag{15}$$

The initial condition imposed is presented in (16).

$$\Psi^{(1)} = 0 \quad \text{on} \quad t = 0\,\text{s} \tag{16}$$

From now on, the superscript $^{(1)}$ denoting the first order quantities of the formulation will be suppressed in order to simplify the notations.

2.2. Numerical method

In order to solve the initial boundary value problems defined for the velocity and acceleration potentials, the present TDRPM adopts a low order boundary element method using the Rankine's source as Green's function G_{PQ}:

$$G_{PQ} = \frac{1}{\sqrt{(x_p - x_q)^2 + (y_p - y_q)^2 + (z_p - z_q)^2}}, \tag{17}$$

where P and Q are field and source points, respectively.

In this method, the integral equations for the velocity and acceleration potentials, presented in Eqs. (18) and (19), are solved at a certain time step, whereas a fourth order Runge–Kutta method (RK4) time marching scheme is applied to update the boundary conditions to a new time step.

$$\iint_{\partial\Omega'_{-P}}\left[\phi_Q\frac{\partial G_{PQ}}{\partial n_Q} - G_{PQ}\frac{\partial\phi_Q}{\partial n_Q}\right]\mathrm{d}\partial\Omega' = \begin{cases} -4\pi\phi_P & \text{if } P \text{ inside } \Omega', \\ -2\pi\phi_P & \text{if } P \text{ is at } \partial\Omega', \\ 0 & \text{if } P \text{ is outside } \Omega', \end{cases} \tag{18}$$

$$\iint_{\partial\Omega'_{-P}}\left[\Psi_Q\frac{\partial G_{PQ}}{\partial n_Q} - G_{PQ}\frac{\partial\Psi_Q}{\partial n_Q}\right]\mathrm{d}\partial\Omega' = \begin{cases} -4\pi\Psi_P & \text{if } P \text{ inside } \Omega', \\ -2\pi\Psi_P & \text{if } P \text{ is at } \partial\Omega', \\ 0 & \text{if } P \text{ is outside } \Omega'. \end{cases} \tag{19}$$

Aiming at guaranteeing a stable evolution of the solution until the achievement of a steady-state, the numerical scheme also considers the use of a ramp function $f_r(t)$ defined by:

$$f_r(t) = \begin{cases} \frac{1}{2}\left[1 - \cos\left(\frac{\pi t}{T_r}\right)\right] & \text{if } t \le T_r \\ 1 & \text{if } t > T_r \end{cases}. \tag{20}$$

where T_r is the ramp time which is set as a multiple of a characteristic wave period involved in the simulations.

Moreover, in order to prevent the diffracted waves reaching the free surface boundaries and being reflected back to the bodies positions, the numerical damping zone concept, firstly proposed by Israeli and Orszag [10], is imposed near the free surface edge. Among several variations of the method that may be observed in the literature, such as the ones applied in Prins [11], Bunnik [12], Boo [13] and Shao [14], in this work the formulation applied by Zhen et al. [15] has been used:

$$\frac{\partial\eta}{\partial t} = \frac{\partial\phi}{\partial z} - \nu(x,y)\eta \quad \text{at} \quad z = 0 \quad \text{and} \quad \sqrt{x^2+y^2} > L_{dz}, \tag{21}$$

$$\frac{\partial\phi}{\partial t} = -g\eta - \nu(x,y)\phi \quad \text{at} \quad z = 0 \quad \text{and} \quad \sqrt{x^2+y^2} > L_{dz}, \tag{22}$$

in which L_{dz} is the distance between the center of the free surface circular mesh and the begining of the damping region and $\nu(x,y)$ is a function that defines the dissipation characteristic of this region, described by:

$$\nu(x,y) = a\omega\left(\frac{\sqrt{x^2+y^2} - L_{dz}}{b\lambda}\right)^2, \tag{23}$$

where a defines the intensity of dissipation and b the damping zone length. These values must be tuned by preliminary tests in order to avoid the occurrence of reflected waves which may spoil the solution. In general, we observe that the damping zone must have a minimum length of one wave length, $b = 1$, whereas the intensity must be set in such a way that permits a progressive and smooth dissipation of the waves. Damping zones with large values of a (i.e. $a \ge 3$) may behave as a fixed wall.

In Watai et al. [16], the TDRPM code was applied to solve the seakeeping problem of two ships arranged in side-by-side. This study was motivated by the application of the code to the offloading process of the so-called floating liquefied natural gas (FLNG) units and liquefied natural gas (LNG) carriers. During the operation, the relative distance between the vessels remains almost constant for it is maintained by a pre-tensioned mooring arrangement comprised by anchor lines and pneumatic fenders placed in-between the ships. Therefore, from the computational point of view, both vessels can be discretized considering fixed panel meshes around their mean

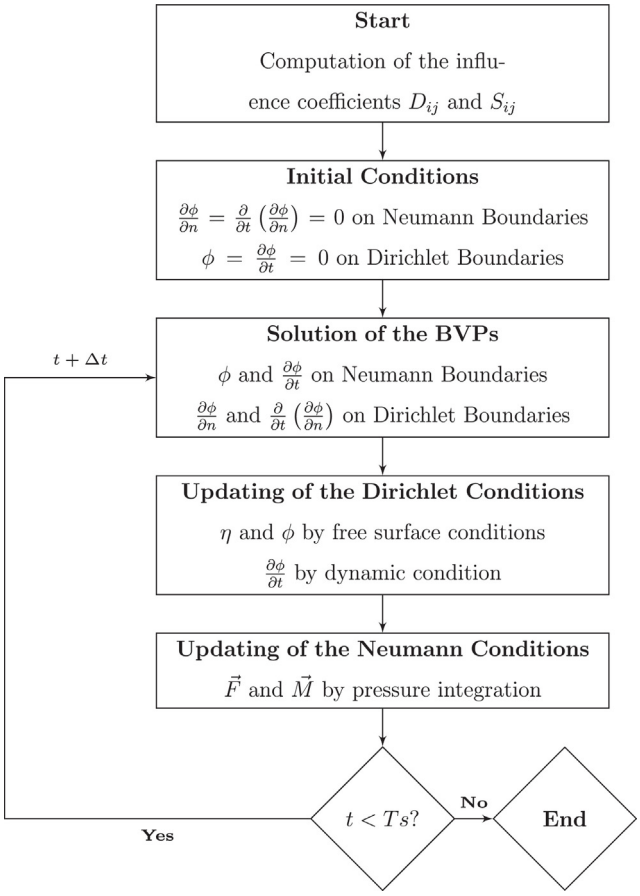

Fig. 1. Flowchart structure of the numerical method.

positions. This approach greatly reduces the computational efforts since the influence matrices can be calculated just once and prior to the beginning of the time loop of the simulation. The procedure is exemplified in the flowchart of the code presented in Fig. 1, in which S_{ij} and dipole D_{ij} are known in the literature as the source and dipole influence coefficients, respectively.

However, as mentioned before, when dealing with multi-body problems that are prone to large horizontal displacements, the same computational strategy for solving the seakeeping problem cannot be applied, mainly due to the fact that now the transient hydrodynamic interactions that results from changes in the relative positions must be taken into account. For coping with this kind of problems, the TDRPM code has been improved with a numerical procedure that couples the hydrodynamic solver with a re-meshing and a free surface interpolation algorithm, enabling the change of relative positions of the vessels along each simulation.

This first version of the code only considers linear wave effects, and therefore mean loads such as the mean drift forces are not taken into account in the dynamics of the vessels. Other external forces such as those arising from wind, current or self propulsion of the vessels are also not included in the numerical model. As a consequence, the relative displacements are introduced only as prescribed motions.

Although the solutions of first order problem can be used to derive second order contributions, it is known that a low order approach is not the most appropriate for the computation of mean, slow and wave-current interaction loads, since they all require accurate computation of the derivatives of the velocity potential. In order to overcome this limitation and thus enable future applications of the code for more generic problems, the TDRPM is currently being reformulated in a higher order approach, in which the body

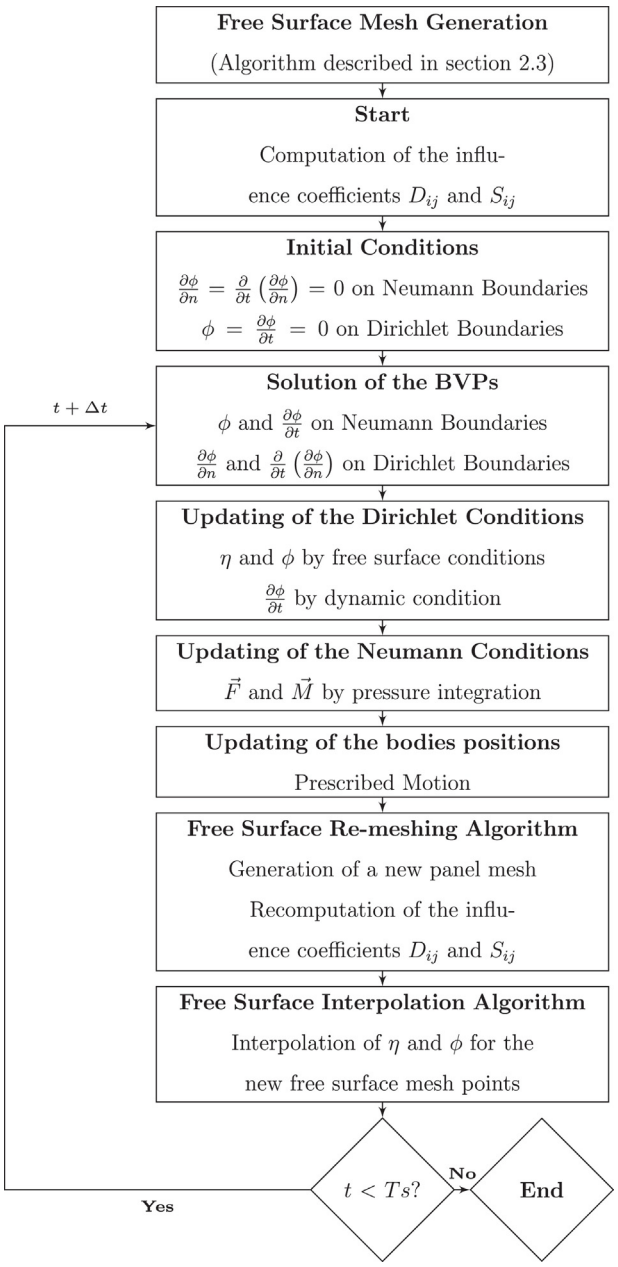

Fig. 2. Flowchart of the structure of the numerical method including the re-meshing and interpolation algorithms in the time loop.

geometry and the computed functions will be described using non-uniform rational basis splines (NURBS) and B-splines, respectively. The first results of this development can be observed in Ruggeri et al. [17]. With this future version of the code, the slow horizontal motions of the bodies could be determined during the simulations by solving the bodies' equation of motion and by applying a wave filter with the purpose to separate the first order frequency oscillatory induced motions from the ones caused by slowly varying disturbances. In this sense, it is important to emphasize that the proper choice of the wave filter is crucial to avoid significant introduction of phase lag into the solution, which tends to cause instabilities to the algorithm. An interesting study concerning the application and comparison of different alternatives of wave filters is presented in Tannuri et al. [18], from which one may extract that both the cascaded notch filter and Kalman filters may be promising alternatives to be applied to the problems we are planning to deal with.

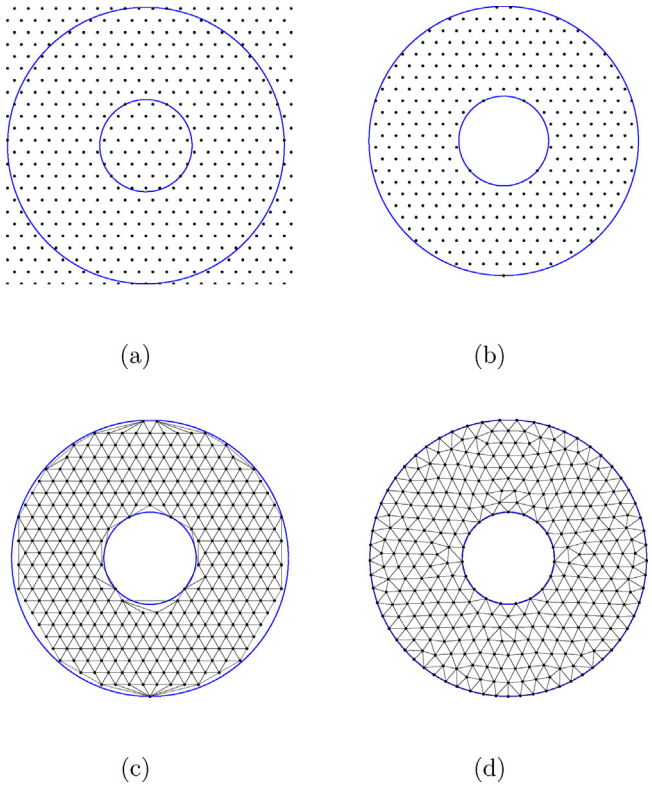

Fig. 3. Steps of the mesh generation algorithm applied to a circular surface with radius $R = 3$ m with a circular of radius $R = 1$ m inside. (a)–(c) The first three steps of the algorithm loop structure. (d) The final mesh.

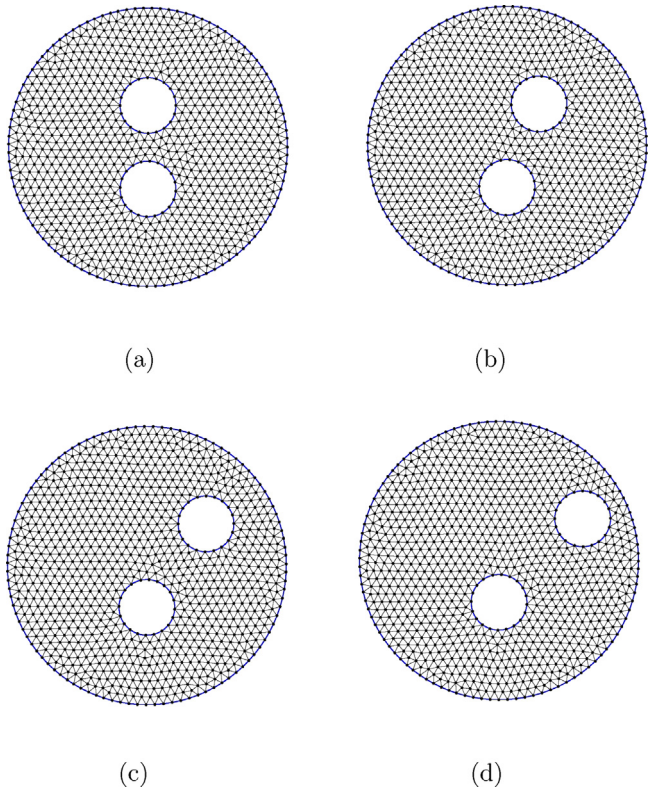

Fig. 4. Four circular meshes of radius $R = 5$ m with two circular apertures of radius $R = 1$ m in different relative distances.

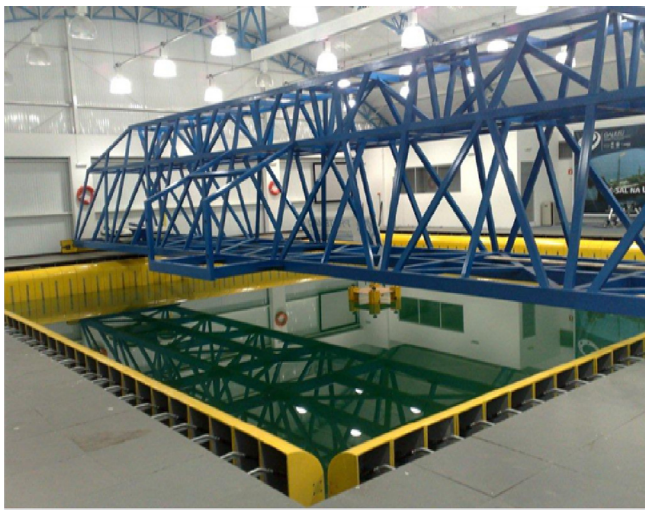

Fig. 5. Hydrodynamic Calibrator of the Numerical Offshore Tank of the University of Sao Paulo (CH-TPN-USP).

Therefore, in the absence of mean forces, for now the relative displacements are introduced only as prescribed motions. In addition, it is supposed that the large prescribed displacements are sufficiently slow not to generate waves by themselves. As a consequence, the problem may be treated in a quasi-static manner regarding the low-frequency displacement, while maintaining the linear characteristic of the code. The approach also makes it possible to retain the numerical methods for solving the IBVPs that were already described in item 2. The flowchart structure of the new method is presented in Fig. 2. Next a description of the free surface re-meshing and interpolation algorithms is presented.

2.3. The free surface re-meshing algorithm

A simulation involving large relative displacements between two or more bodies requires a special treatment of the free surface, since the wave elevation and the velocity potential must be defined at new horizontal positions as the bodies move. Different alternatives to handle this problem could be applied including: a fully Lagrangian description of the free surface, in which the free surface nodes are identified as material particles [19]; a semi-Lagrangian formulation in which the horizontal motion of free surface nodes is prescribed [20,21]; and also the re-gridding method, which generates free surface nodes for each time-step of the simulation. Depending on the problem, one of the techniques may be easier to apply than the others. In the context of the present three-dimensional low order method, the application of the fully Lagrangian or the semi-Lagrangian methods would lead to additional difficulties associated to the calculation of the spatial gradients of the velocity potential and, for the latter, of the free surface elevation. Therefore, the re-gridding method was adopted, for being the one with most direct application to our code.

The re-meshing algorithm developed in this work is merely an adaptation of the 2D mesh generator elaborated by Persson [22], entitled in his work “A Simple Mesh Generator in MATLAB”. Only simple adaptations were made, which were required for including the algorithm in the time domain loop of the TDRPM code. Persson’s algorithm was chosen for its simplicity, which rendered its integration to the code relatively straightforward if compared to other meshing software that are often much more complex.

Persson [22] fully describes the mesh generator algorithm and how it may be implemented computationally. The main idea of the method is to consider the force magnitude at the joints based on a simple repulsive force model for each structure bar. For the sake

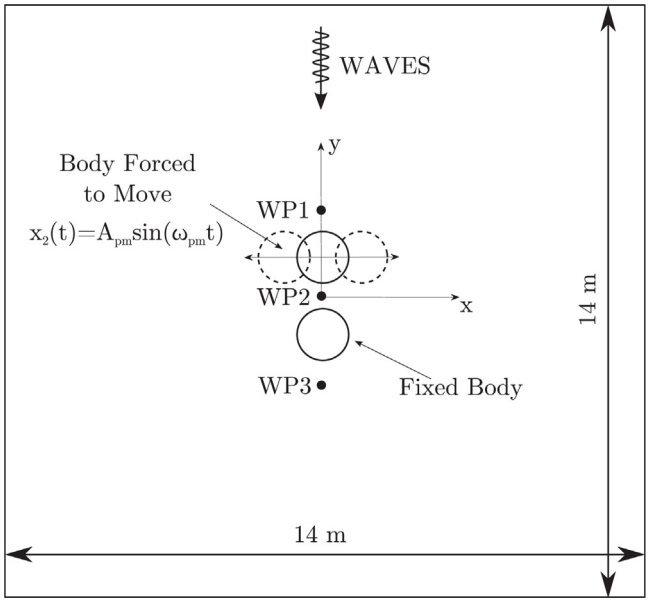

Fig. 6. Illustrative sketch of the experimental setup.

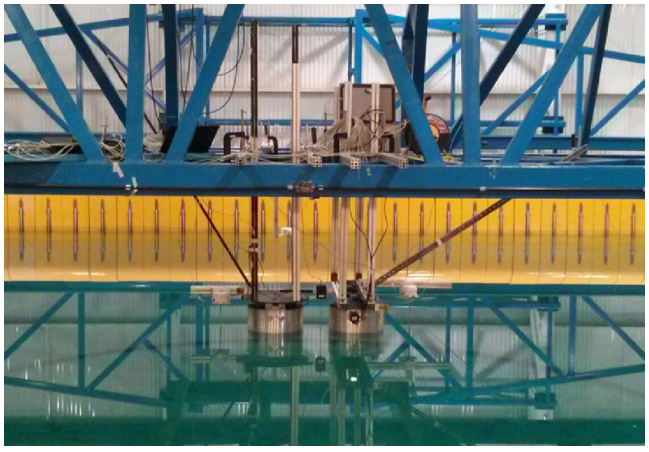

Fig. 7. Lateral view of the models positioned in the tank.

of completeness, only a brief description for the comprehension of the method will be exposed here. The simplified loop structure of the mesh generator is described in the following items:

1. Creation of a uniform distribution of mesh points within a bounding box that covers a pre-specified surface;
2. Removal of all points outside the desired geometry surface;
3. Determination of the truss topology by a Delaunay triangulation and calculation of the structure bars lengths;
4. Calculation of the force magnitude at the joints of each structure bars;
5. Calculation of the force components at the joints of each structure bars;
6. Solve a equilibrium equation for updating of the node positions;
7. If a point ends up outside the surface after the update of node positions, it is moved back to the closest point on the boundary.
8. The last positions are compared with the previous ones and if non "large movements" are detected (specified criteria) the algorithms is stopped, otherwise the algorithm is restarted in item 3, continuing until the criteria is satisfied.

Application of the algorithm may be exemplified by applying it to the generation of a circular mesh of radius $R = 3$ m with a circular

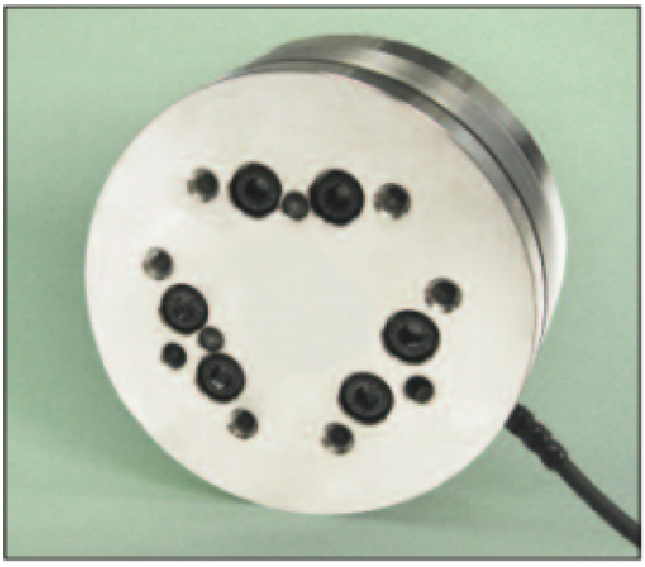

Fig. 8. ATI MINI85 6 D.O.F. load cell.
Source: ATI Catalog.

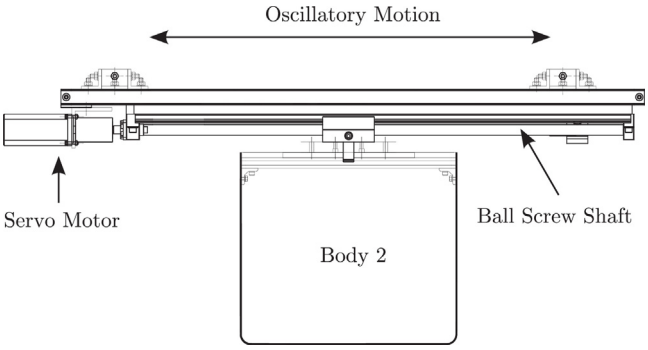

Fig. 9. Sketch of the mechanical equipment attached to Body 2.

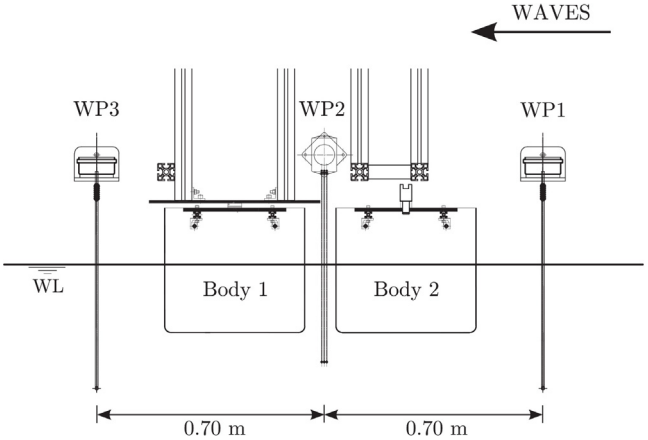

Fig. 10. Lateral view sketch of the models and wave probes arrangement.

aperture of radius $R = 1$ m inside. Fig. 3(a)–(c) illustrates the first three steps of the algorithm, whereas Fig. 3(d) presents the final mesh, it means, when the system $F(p) = 0$ is satisfied.

Next, Fig. 4 presents four circular meshes of radius $R = 5$ m with two circular apertures of radius $R = 1$ m in different relative positions, illustrating the algorithm capability for dealing with the generation of free surface meshes that may be applied to hydrodynamic problems involving two diffrent bodies. These meshes

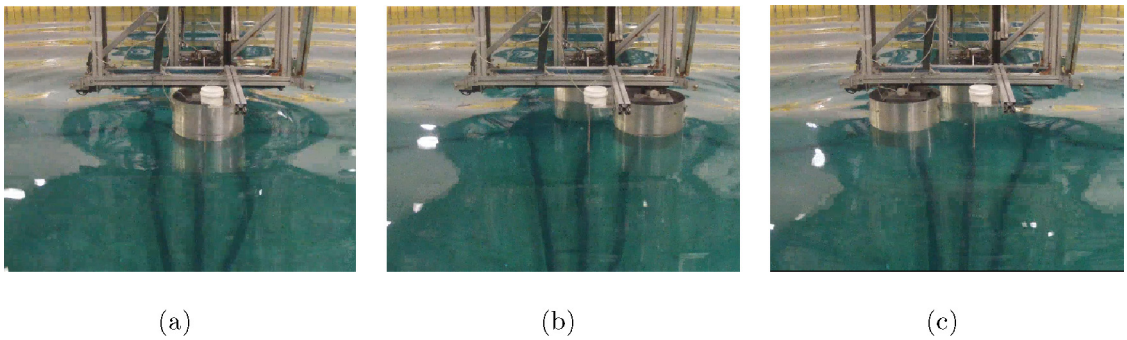

Fig. 11. Video frames recorded during the tests with a regular wave of frequency $\omega_l = 7.2$ rad/s and Body 2 oscillation frequency $\omega_{pm} = 0.48$ rad/s. Instants (a) $t = t_o$, (b) $t = t_o + T/4$ and (c) $t = t_o + 3T/4$.

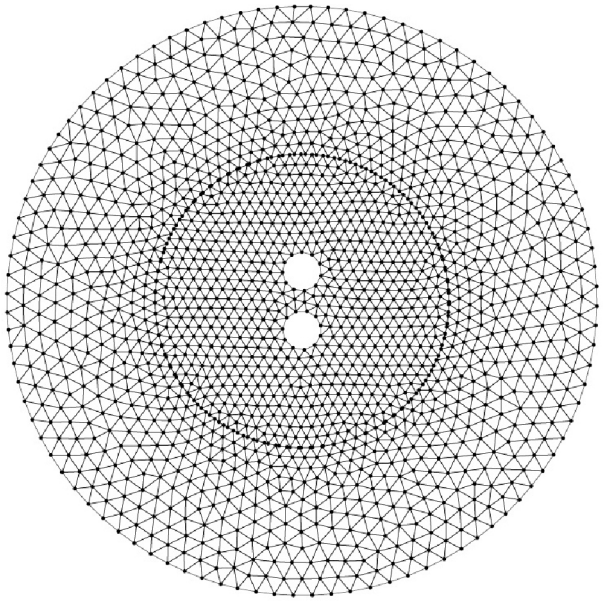

Fig. 12. Free surface mesh for wave Reg 1. Wave frequency $\omega_l = 6.4$ rad/s.

represent four different instants of a simulation involving two circular cylinders, in which the trajectory of one of them was prescribed to perform a large horizontal displacement. It is worth mentioning that these meshes are not restricted to cases considering only bodies with circular cross-sections, since other geometries such as ship-shaped vessels, for example, could be surrounded by circular meshes that fit right into the circular apertures.

2.4. The free surface interpolation algorithm

As remarked in Section 2.3, as the free surface is re-meshed, new collocation points (centroid of each triangle) are generated, but, unfortunately, neither the free surface elevation nor the velocity potential are known in these new points, and the simulation cannot continue.

In order to overcome this problem, it is necessary to apply an interpolation scheme to link the mesh generator to the flow solver, so as to allow the simulation to be restarted from a previous free surface state. More precisely, after generating a new mesh, the interpolation scheme must recover, as accurately as possible, the previous solution field defined on the old mesh to proceed with the computation.

The choice of the interpolation scheme must be done carefully, since an inadequate selection may be a source of error

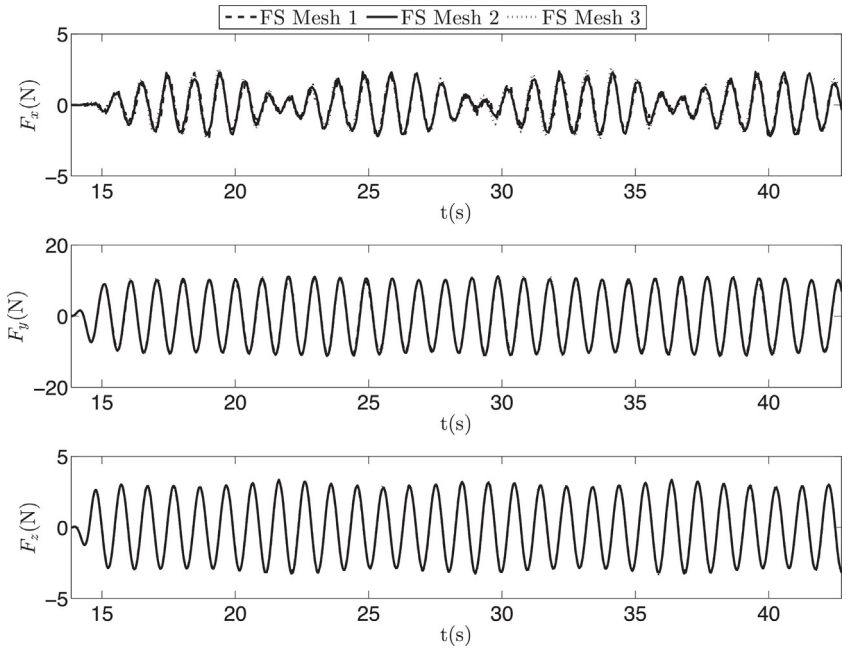

Fig. 13. Case 1: Convergence analysis of the hydrodynamic forces F_x, F_y and F_z.

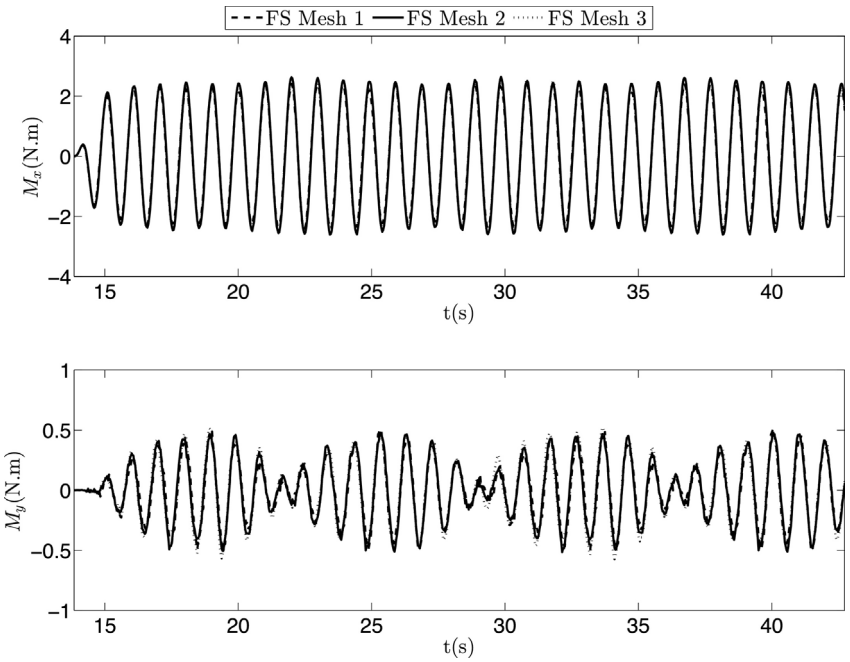

Fig. 14. Case 1: Convergence analysis of the hydrodynamic moments M_x and M_y.

that, in time-dependent problems, will accumulate throughout the simulations. Therefore, linear interpolation methods are normally avoided in favor of higher order schemes. With this in mind, we have implemented an interpolation scheme that couples a second order polynomial to a weighted moving least-squares method. This method is similar to the one applied by Wang [23].

In this scheme, the shape of the free surface elevation and the velocity potential distribution are represented by the second order polynomials presented in Eq. (24)

$$\eta = F_\eta(x, y) = a_1 + a_2x + a_3y + a_4x^2 + a_5xy + a_6y^2 \tag{24a}$$

$$\phi = F_\phi(x, y) = b_1 + b_2x + b_3y + b_4x^2 + b_5xy + b_6y^2 \tag{24b}$$

in which, fixing to one point in space p_0, the 12 coefficients a_i, b_i, $i = 1, 2, 3, \ldots, 6$ of the polynomials are calculated considering only the nearest points within a distance of $2l_0$, where l_0 is the local mesh size. Denote these nearest points as p_k, $k = 1, 2, 3, \ldots, N_{np}$, in which N_{np} is the number of points.

Thus, the coefficients are determined by using a weighted moving least-squares method with the error function given by:

$$\sigma(a_1, a_2, a_3, a_4, a_5, a_6) = \sum_{j=1}^{N_{np}} W_k[F_\eta(x_k, y_k) - \eta_k]^2 \quad N_{np} \geq 6 \tag{25a}$$

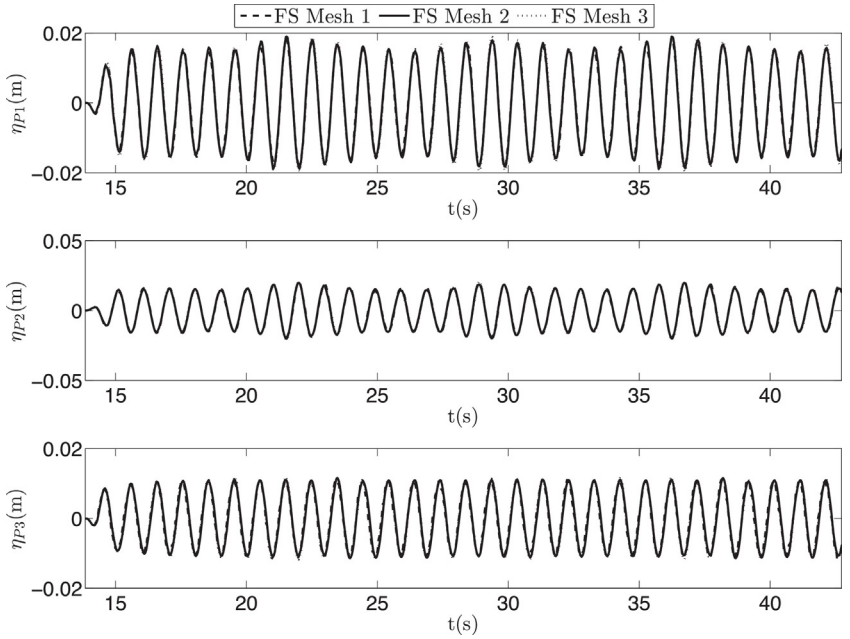

Fig. 15. Case 1: Convergence analysis of the wave elevations at WP1, WP2 and WP3.

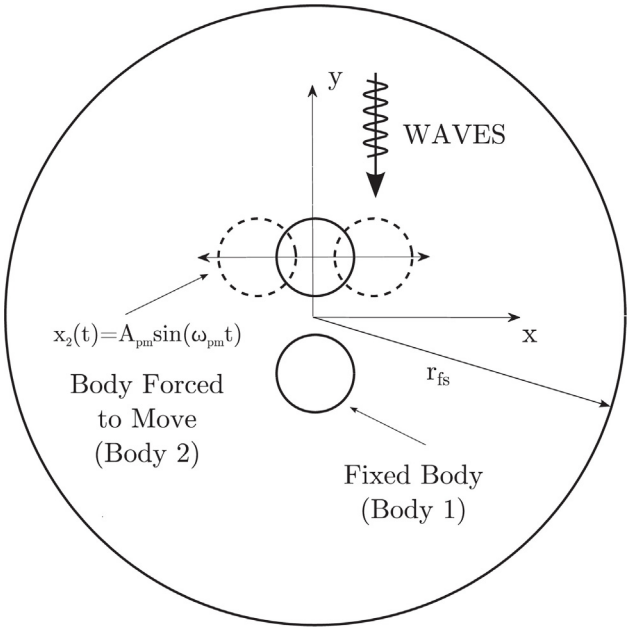

Fig. 16. Illustrative view of the numerical setup.

$$\sigma(b_1, b_2, b_3, b_4, b_5, b_6) = \sum_{j=1}^{N_{np}} W_k [F_\phi(x_k, y_k) - \phi_k]^2 \quad N_{np} \geq 6 \tag{25b}$$

in which W_k, see expression (26), is the weight function for the nearest points p_k. Notice that the weight function decreases exponentially with the distance between p_k and the point p_0.

$$W_k = e^{-\frac{|p_k - p_0|}{2l_0}} \tag{26}$$

In accordance to the least-squares method, let $\partial\sigma/\partial a_j = 0$ and $\partial\sigma/\partial b_j = 0$, thus obtaining a linear system of equations (27) for a_j and b_j.

$$\sum_{j=1}^{6} A_{\eta ij} a_j = B_{\eta i} \quad i = 1, 2, 3, \ldots, 6 \tag{27a}$$

$$\sum_{j=1}^{6} A_{\phi ij} b_j = B_{\phi i} \quad i = 1, 2, 3, \ldots, 6 \tag{27b}$$

A_η, A_ϕ, B_η and B_ϕ are defined by the expressions (28):

$$A_{\eta ij} = A_{\phi ij} = \sum_{k=1}^{N_{np}} W_k \beta_{kj} \beta_{ki} \tag{28a}$$

$$B_{\eta ij} = \sum_{k=1}^{N_{np}} W_k \eta_k \beta_{ki} \tag{28b}$$

$$B_{\phi ij} = \sum_{k=1}^{N_{np}} W_k \phi_k \beta_{ki} \tag{28c}$$

Finally, the coefficients β are calculated by the following expressions:

$$\beta_{k1} = 1 \quad \beta_{k2} = x_k \quad \beta_{k3} = y_k \tag{29}$$

$$\beta_{k4} = x_k^2 \quad \beta_{k2} = x_k y_k \quad \beta_{k3} = y_k^2 \tag{30}$$

in which $k = 1, 2, 3, \ldots, N_{np}$.

The coefficients a and b that result from this interpolation scheme are determined from one mesh, here denoted as current mesh, in which the free surface elevation and the velocity potential distribution are known. Hence, after the positions of the bodies are changed and the re-meshing of the free surface is performed, the polynomials (24) are used to determine the desired quantities at the new grid points. In case new grid points appear at new mesh

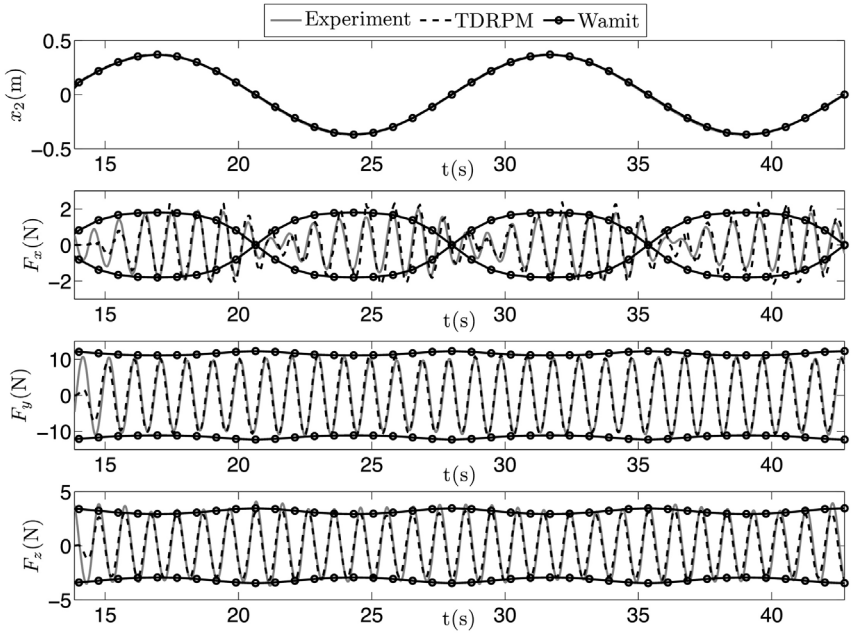

Fig. 17. Case 1: Comparison of numerical and experimental results in terms of position of Body 2 in time and the associated time series of the hydrodynamic forces F_x, F_y and F_z.

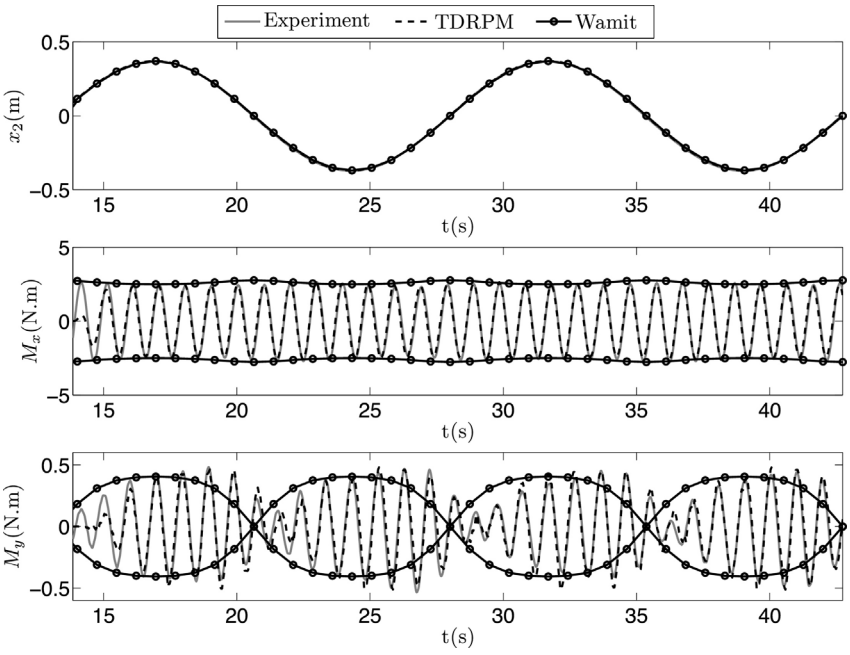

Fig. 18. Case 1: Comparison of numerical and experimental results in terms of position of Body 2 in time and the associated time series of the hydrodynamic moments M_x and M_y.

areas, as for example, those that were previously located inside the bodies, the algorithm simply extrapolates the desired quantities using the polynomial computed with the ten nearest points. Since the polynomials are calculated by a weighted moving least-square method, the value of the unknown point approaches the value of the nearest point of the current mesh, which tends to reduce the extrapolation errors if the meshes are dense enough at this region and if the position of the bodies does not change abruptly from one time-step to another, which in practice is guaranteed by applying small time-steps and by dealing with problems in which the relative position of the bodies does not change fast.

3. Verification of numerical computation

Numerical simulations considering two bodies with one of them fixed and the other undergoing large displacements during the time domain calculations are presented in the following sections. The main objective of this study is to evaluate the hydrodynamic interaction between the bodies in a scenario where the mean horizontal relative positions of the bodies vary in time. With this approach, the wave shielding effects caused by one of the bodies on the other are taken into account and their effects on the hydrodynamic forces can be quantified.

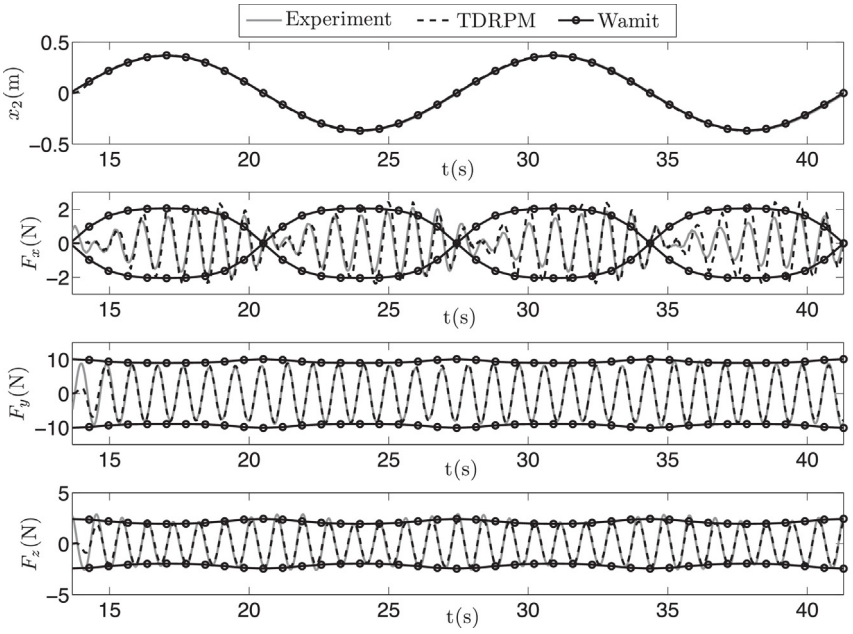

Fig. 19. Case 4: Comparison of numerical and experimental results in terms of position of Body 2 in time and the associated time series of the hydrodynamic forces F_x, F_y and F_z.

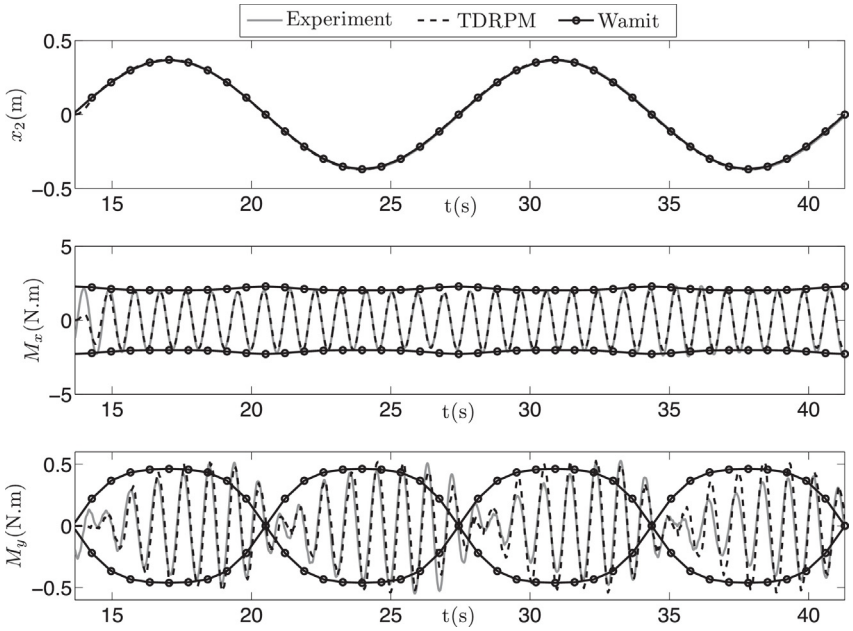

Fig. 20. Case 4: Comparison of numerical and experimental results in terms of position of Body 2 in time and the associated time series of the hydrodynamic moments M_x and M_y.

Once the objectives are established, the study is performed with a set of simulations considering only diffraction effects, it means, the bodies are restrained to oscillate in their six degrees of freedom. In this case, one of the bodies is displaced horizontally from its initial position, performing a slow oscillatory motion with large amplitude.

However, it must be emphasized that the verification of the results is not a simple task, since neither numerical nor experimental results considering such scenario could be found in the literature. The frequency domain software WAMIT will be used only for providing basis of comparison in a quasi-static approach. Obviously, it cannot be directly applied for this problem for it assumes that the mean position of the bodies is constant.

Bearing this in mind, a set of dedicated experimental tests was designed and conducted aiming specifically at verifying the performance of the numerical method for a multi-body system with bodies undergoing large relative displacements. The tests were carried out at the Hydrodynamic Calibrator of the Numerical Offshore Tank of the University of Sao Paulo (CH-TPN-USP), as described next.

3.1. Hydrodynamic Calibrator of USP (CH-TPN-USP)

CH-TPN-USP is a square wave basin with dimensions 14 m × 14 m and water depth of 4 m capable to generate and absorb regular and irregular waves. This tank is equipped with a set of 148 active hinged flap wave makers, each of them driven by a servo-motor and a ball-screw mechanism, and equipped with an ultrasonic wave-sensor for feedback to the absorption algorithm. The algorithm calculates the motions of the wave makers to generate and absorb the required wave field by taking into account the layout of the flaps, the limits of wave generation and also the experimental transfer function that relates the flap amplitude to the wave elevation amplitude. The details of CH-TPN-USP as well as the control system implemented can be observed in Mello et al. [24,25]. A perspective view of the wave basin is illustrated in Fig. 5. In the experiments presented next, one of the tank walls operated in a generation and absorption mode, whereas the other three worked only in absorption mode.

Table 1
Main characteristics of the 6 D.O.F. load cell.

Calibration SI-1900-80				
Forces/moments	F_x, F_y (N)	F_z (N)	M_x, M_y (Nm)	M_z (Nm)
Sensing ranges	1900	3800	80	80
Single-axis-overload	13,000	27,000	500	610

3.2. Experimental setup

The experimental tests considered a multi-body system comprising two identical aluminum circular cylinders, namely Body 1 and Body 2, with 0.40 m of diameter, 0.36 m of height. Both were tested with a draught of 0.20 m. Figs. 6 and 7 present an illustrative sketch and a photograph of the experimental setup, respectively.

Tests were conceived in a very fundamental configuration with the main goal of providing benchmark data for the present numerical method. Thus, during the tests the Body 1 was kept fixed and connected to a 6 D.O.F. load cell (see Fig. 8) that measured the hydrodynamic forces and moments induced by the waves. In addition, this load cell was properly positioned in the model in order to follow the sign convention of the coordinate system presented in Fig. 6. The main particulars of the load cell are presented in Table 1.

Body 2 was positioned upstream of Body 1 and was attached to a ball screw shaft driven by a servo motor, this system being used to impose the prescribed oscillatory motion on the body during the measurements, as illustrated in Fig. 9. Moreover, this mechanical device was also equipped with a resistive potentiometer, which enabled one to monitor Body 2 position in a synchronized manner with the forces and moments measured on Body 1. The procedure provided a convenient and controlled setup for the multi-body system for the sake of the numerical modeling of the problem.

Three wave probes, namely WP1, WP2 and WP3, were used to measure the wave elevations at different locations near the bodies. WP2 was placed at the mean position between the bodies, while WP1 and WP3 were positioned upstream and downstream, respectively. The positions of the wave probes are presented in Fig. 10.

Special care had to be taken for the definition of the wave frequencies to be considered in this test. One must keep in mind the difficulties associated with measuring interaction forces induced

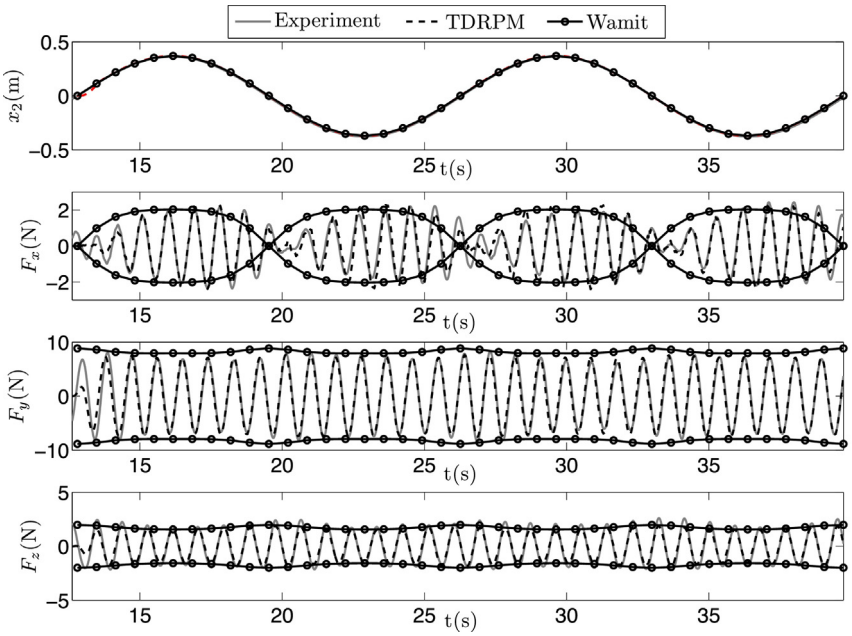

Fig. 21. Case 7: Comparison of numerical and experimental results in terms of position of Body 2 in time and the associated time series of the hydrodynamic forces F_x, F_y and F_z.

by waves diffracted from the bodies, which are commonly much lower than those caused by the incident wave itself. Thus, small interferences from reflected waves coming from the tank walls may disturb the results, demanding a good performance of the CH-TPN's active control system that should absorb these waves. As reported by Mello et al. [24], the system has a better performance when absorbing waves in the range of frequencies between 3.14 rad/s and 7.5 rad/s and, therefore, the wave frequencies were all selected within this range. In addition, since this experimental campaign was conducted focusing on the verification of the linear numerical method, the tests considered only regular waves of small amplitude and steepness ($H/\lambda \leq 2\%$), which were previously calibrated in the absence of the models. Only one wave direction was considered (waves propagate in the negative direction of axis y, see Fig. 6) due to physical restrictions for positioning the mechanical device on the tank bridge. In total, 4 regular waves were selected for this test, and their main particulars are presented in Table 2.

Table 2
Regular waves considered in the tests.

ID	ω (rad/s)	T (s)	H (m)	λ (m)
Reg 1	6.400	0.982	0.023	1.506
Reg 2	6.800	0.924	0.020	1.330
Reg 3	7.000	0.898	0.019	1.259
Reg 4	7.200	0.873	0.018	1.190

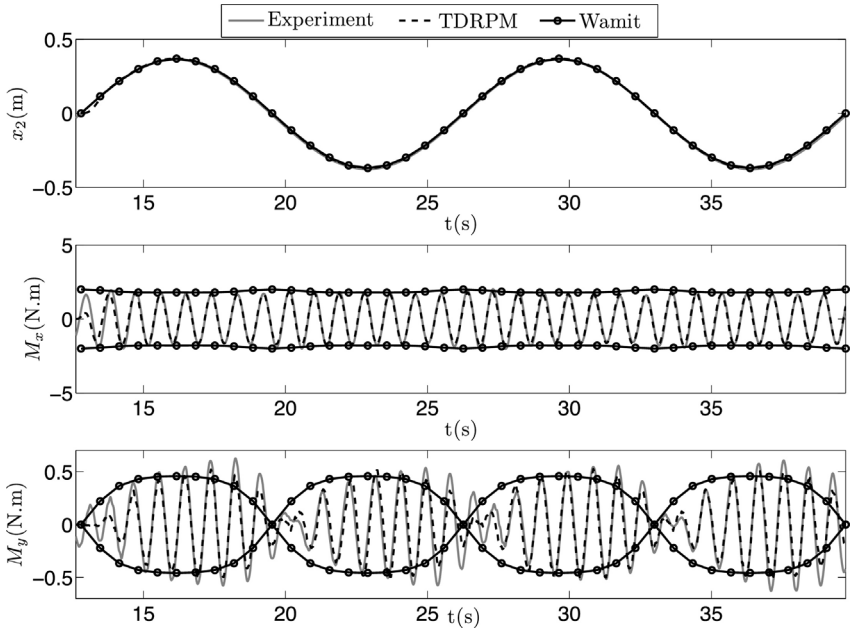

Fig. 22. Case 7: Comparison of numerical and experimental results in terms of position of Body 2 in time and the associated time series of the hydrodynamic moments M_x and M_y.

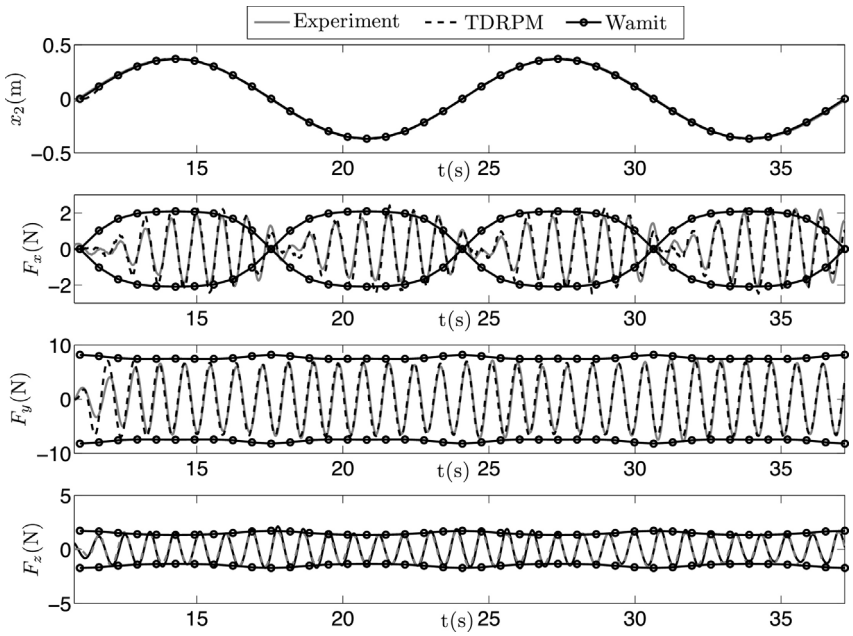

Fig. 23. Case 10: Comparison of numerical and experimental results in terms of position of Body 2 in time and the associated time series of the hydrodynamic forces F_x, F_y and F_z.

All tests begin with the cylinders aligned with respect to the y axis and with a distance of 0.6 m (center-to-center). Once the wavemakers start to move, the servo motor is also activated and Body 2 is horizontally displaced from its initial position with a prescribed oscillatory motion of frequency ω_{pm} and amplitude $A_{pm} = 0.37$ m, this value being the maximum stroke of the ball screw shaft of the mechanical equipment. The oscillation frequency ω_{pm} was defined as a ratio of the incoming wave frequency ω_I. For each regular wave three different oscillation frequencies of Body 2 were considered, these being $\omega_{pm} = \omega_I/15$, $\omega_{pm} = \omega_I/30$ and $\omega_{pm} = \omega_I/60$. The test matrix therefore comprised 12 different cases, listed in Table 3.

A better understanding of the experimental setup may be achieved by observing the pictures in Fig. 11, which displays three video frames recorded during the tests for Case 10. One should notice that at the instant $t = t_o$ (Fig. 11(a)), the two bodies are aligned with respect to the y axis; further on, at $t = t_o + T/4$ (Fig. 11(b)), Body 2 is displaced 0.37 m to right. Finally, at the instant $t = t_o + 3T/4$

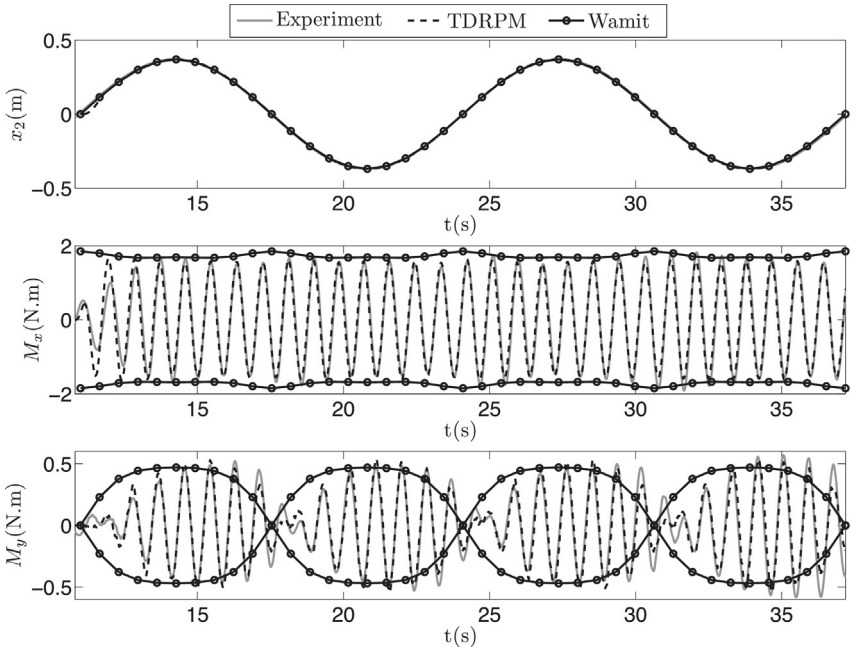

Fig. 24. Case 10: Comparison of numerical and experimental results in terms of position of Body 2 in time and the associated time series of the hydrodynamic moments M_x and M_y.

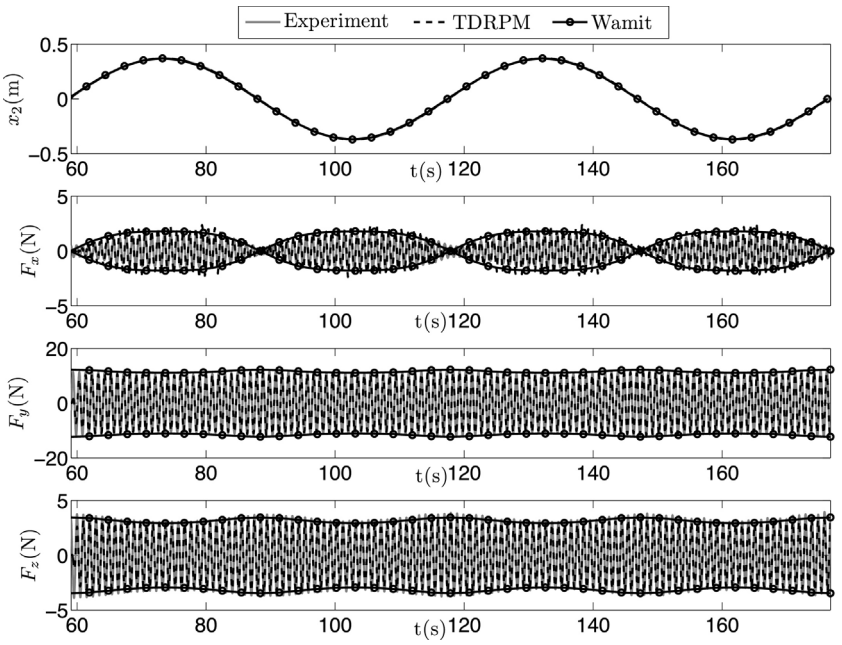

Fig. 25. Case 3: Comparison of numerical and experimental results in terms of position of Body 2 in time and the associated time series of the hydrodynamic forces F_x, F_y and F_z.

(Fig. 11(c)), Body 2 is situated 0.37 m left from its initial position. This sequence of events was repeated four times for each one of the tests in Table 3.

3.3. Numerical grids for the case studies

The numerical simulations were performed with two circular cylinders discretized in 500 quadrilateral panels, a grid that was defined by means of a convergence analysis already presented in Watai et al. [6]. Circular free surface meshes were used for the computations shown next. Nevertheless, since the processing times for the present cases are considerably larger in comparison to the simulations involving only fixed meshes, different free surface meshes were applied for each regular wave frequency. This was done because the radius of the free surface must grow with the wave length and, therefore, a significant number of panels can be saved if the meshes are generated for each specific wave frequency.

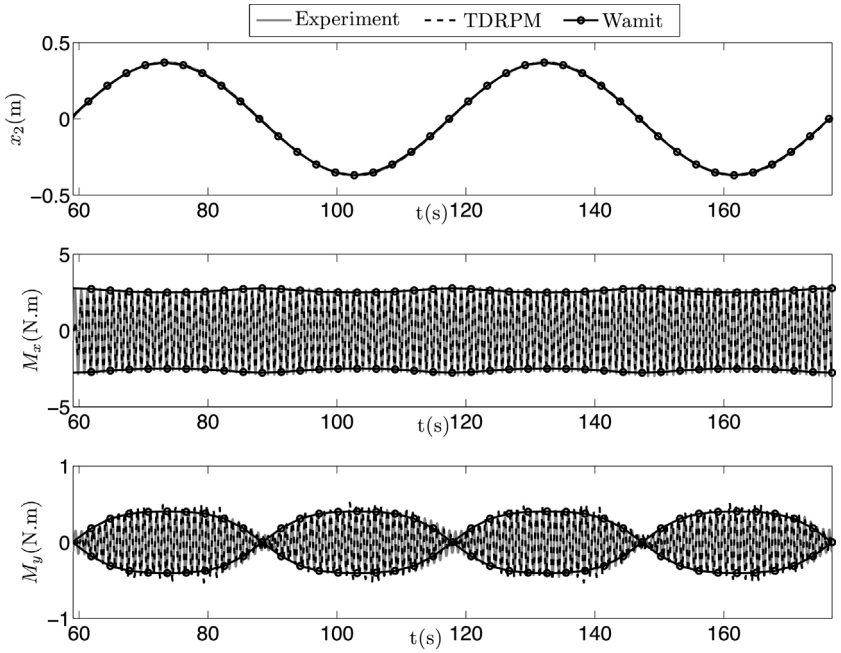

Fig. 26. Case 3: Comparison of numerical and experimental results in terms of position of Body 2 in time and the associated time series of the hydrodynamic moments M_x and M_y.

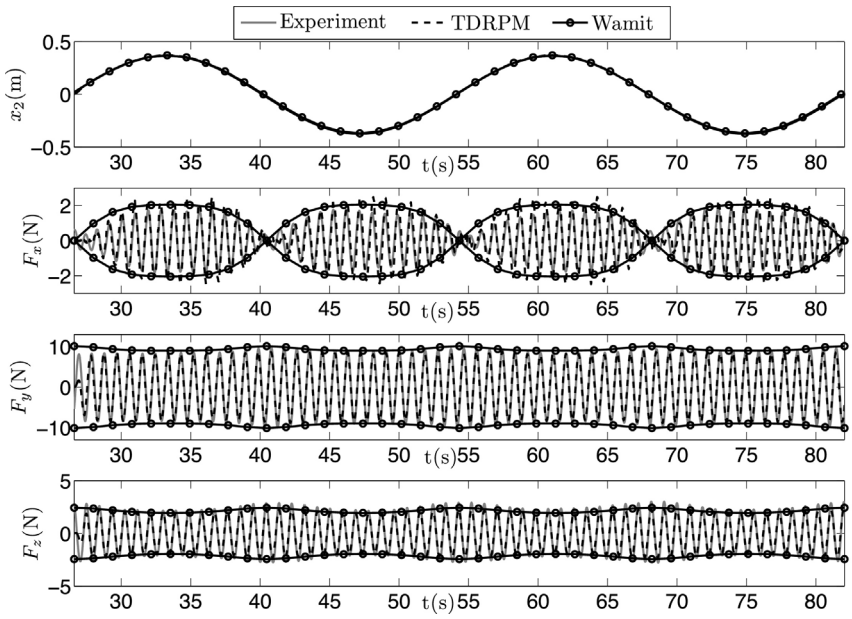

Fig. 27. Case 5: Comparison of numerical and experimental results in terms of position of Body 2 in time and the associated time series of the hydrodynamic forces F_x, F_y and F_z.

For the present calculations, the free surface meshes were constructed with radii of two wavelengths (2λ), in which one wavelength was used for damping the waves through the application of a numerical beach zone. In this part of the mesh, a stretching factor was also applied so as to decrease the panel resolution at regions far away from the bodies. Indeed, this procedure also helped damping the waves, since the numerical dissipation was intensified by the coarse characteristics of the grid in this region. Moreover, this part of the mesh was also kept fixed along the simulations in order to decrease the computational time dedicated to the construction of new meshes at each time step. An example of free surface mesh applied in the computations is presented in Fig. 12.

Figs. 13–15 present an example of convergence analysis performed for Case 1 regarding the hydrodynamic forces, moments and free surface elevations at three different locations. In these figures "FS Mesh 1", "FS Mesh 2" and "FS Mesh 3" refer to three different free surface meshes with 2072, 3010 and 3572 panels, respectively. Although small differences on the time series can be observed when considering the three different free surface meshes, they all present very similar results and, therefore, the employment of the "FS Mesh 2" was judged to be sufficient for the other computations. Similar analyses were also conducted for the other wave frequencies, which resulted in the panel meshes presented in Table 4. It is important to mention that the number of panels

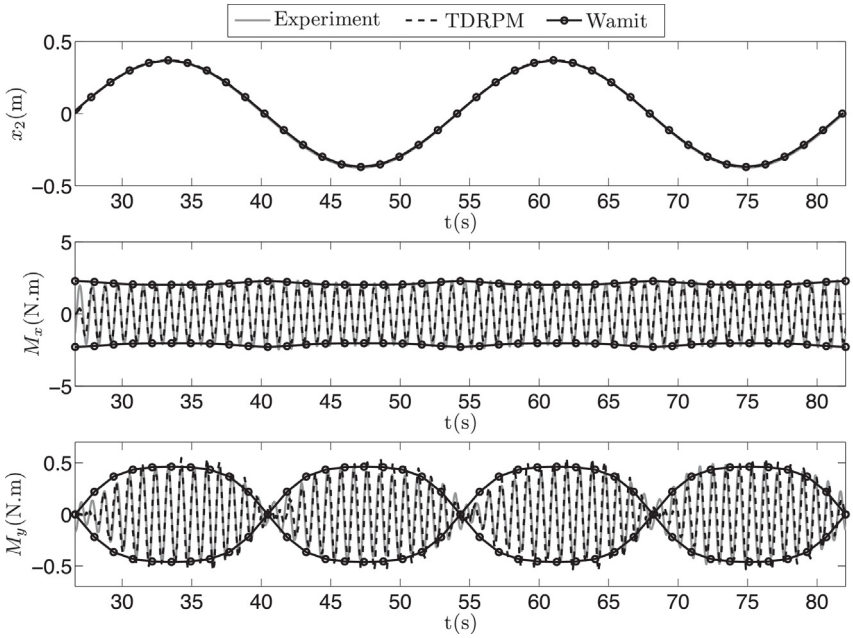

Fig. 28. Case 5: Comparison of numerical and experimental results in terms of position of Body 2 in time and the associated time series of the hydrodynamic moments M_x and M_y.

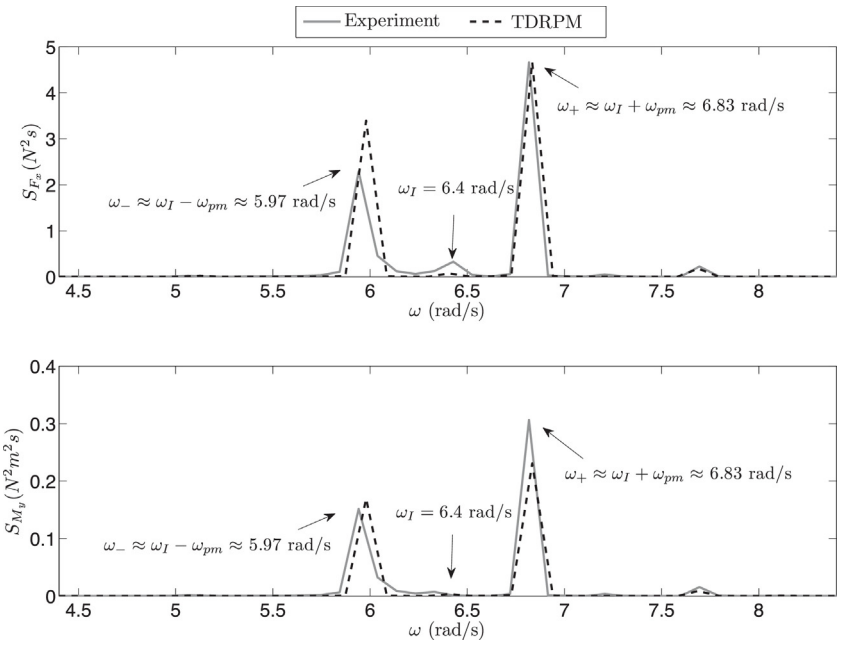

Fig. 29. Case 1: Comparison between present method and experimental data of F_x and M_y response spectra.

indicated in the table represents only a reference value, since the total number of panels is not fixed during the simulations, as the grids are reconstructed for each time step.

The coordinate system adopted for the numerical computations follows the one defined for the experimental tests. For a wave angle of $\theta = 270^\circ$, the waves propagate in the negative direction of axis y, as presented in Fig. 16. A time step of $\Delta t = T/60$ was considered in the simulations.

The simulation begins with a ramp time of $T_r = T$ s in order to avoid the generation of spurious waves into the domain as well as non-physical long transient periods in the solution. All the simulations were run with the amplitudes of the incoming regular waves measured in the experiments.

3.4. Comparison between experimental and numerical results

In this section, the performance of the numerical method is assessed by comparing its predictions to the results measured along the experimental tests. The verification of the numerical results is performed in terms of the hydrodynamic forces on Body 1 and also regarding the wave elevations at the WP positions. For the sake of conciseness, only a set of representative results will be presented, one that includes all the important characteristics observed in both experiments and computations.

Besides the time-series of TDRPM computations and experimental records, the results presented ahead also include steady-state solutions obtained with the frequency domain software WAMIT.

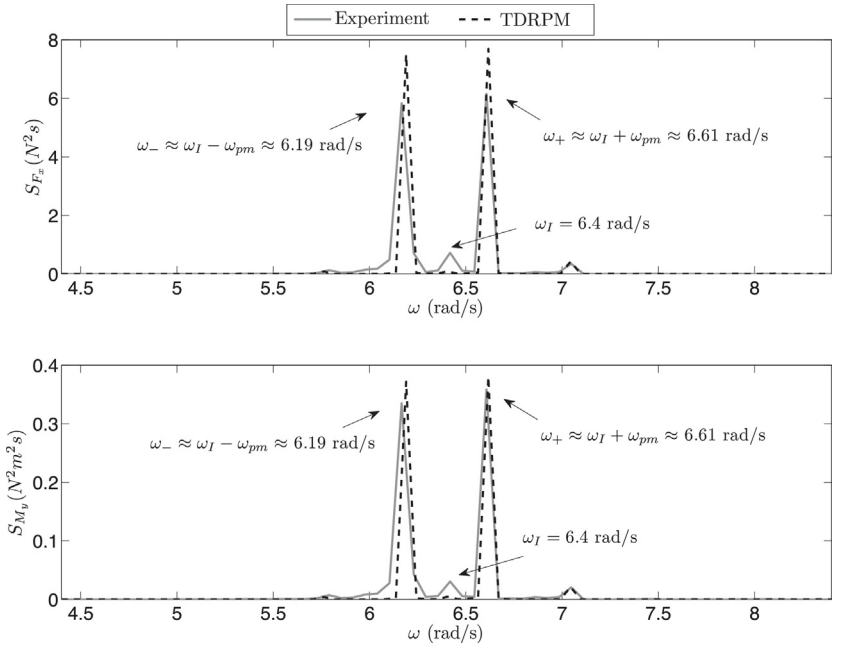

Fig. 30. Case 2: Comparison between present method and experimental data of F_x and M_y response spectra.

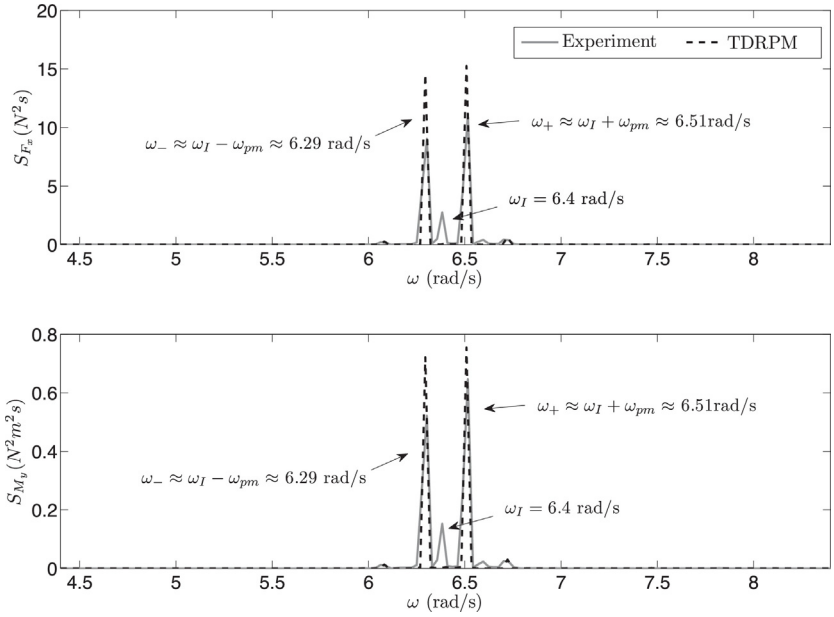

Fig. 31. Case 3: Comparison between present method and experimental data of F_x and M_y response spectra.

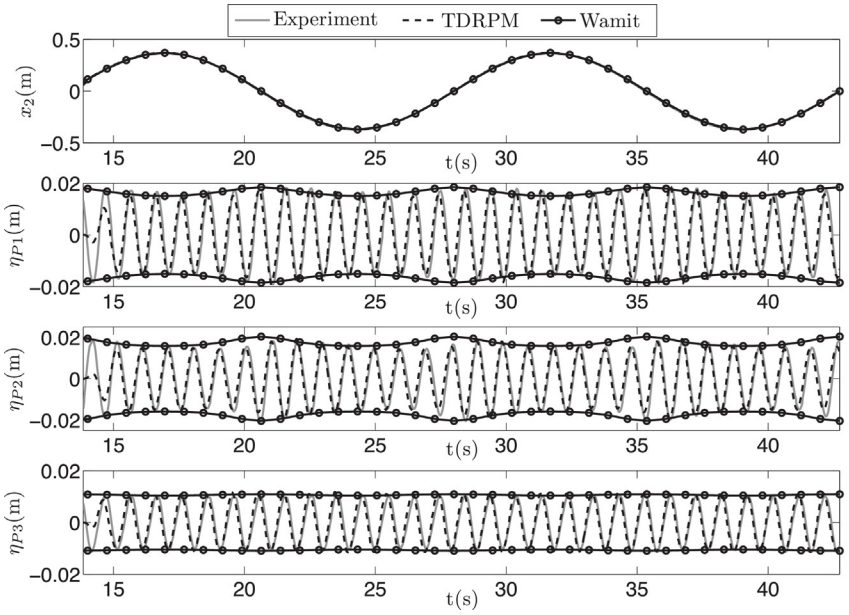

Fig. 32. Case 1: Comparison of numerical and experimental results in terms of position of Body 2 in time and the associated time series of the wave elevations at WP1, WP2 and WP3.

Table 3
Test matrix.

Case	Wave	Oscillator parameters			
		ω_I/ω_{pm}	ω_{pm} (rad/s)	T_{pm} (s)	A_{pm} (m)
1	Reg 1	15	0.427	14.73	0.37
2	Reg 1	30	0.213	29.45	0.37
3	Reg 1	60	0.107	58.90	0.37
4	Reg 2	15	0.453	13.86	0.37
5	Reg 2	30	0.227	27.72	0.37
6	Reg 2	60	0.113	55.44	0.37
7	Reg 3	15	0.467	13.46	0.37
8	Reg 3	30	0.233	26.93	0.37
9	Reg 3	60	0.117	53.86	0.37
10	Reg 4	15	0.480	13.09	0.37
11	Reg 4	30	0.240	26.18	0.37
12	Reg 4	60	0.120	52.36	0.37

These solutions were obtained for several different positions of Body 2 in respect to Body 1. The results were then used to define envelope curves that, by their turn, represent a quasi-static approach. In this regard, the time series obtained in the tests and also with the TDRPM code may be compared to these envelopes in order to evaluate whether or not body nonlinear effects not considered by WAMIT have a significant impact on the results.

Considering Cases 1, 4, 7 and 10 as illustrative examples, Figs. 17–24 present the comparisons between the TDRPM calculations, experimental data and also the envelope amplitude curves provided by WAMIT for the hydrodynamic forces (F_x, F_y and F_z) and moments (M_x and M_y) in Body 1. These cases refer to incident wave frequencies of $\omega_I = 6.4$, 6.8, 7.0 and 7.8 rad/s, and Body 2 oscillation frequencies of $\omega_{pm} = \omega_I/15$ rad/s. These figures also present the motion records of Body 2 in time (x_2), which were used for the

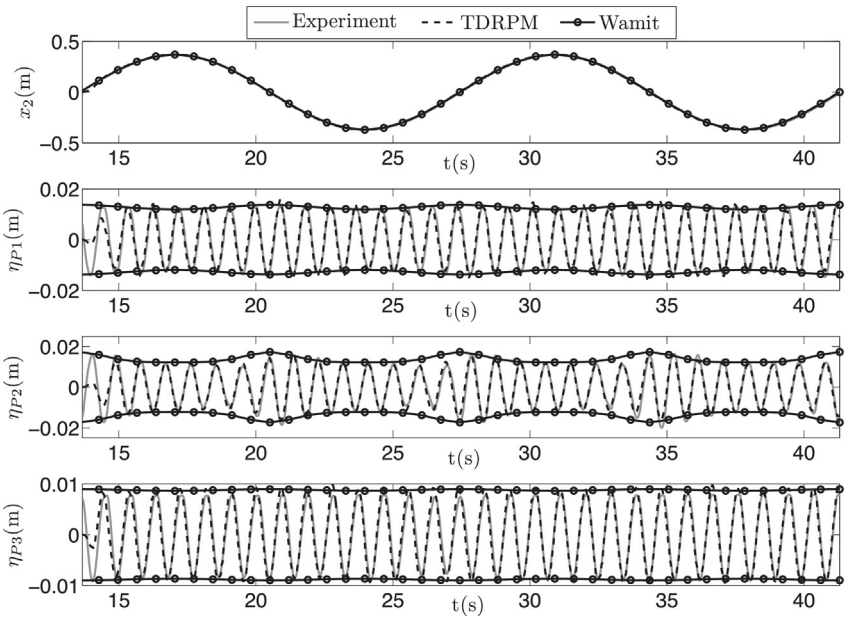

Fig. 33. Case 4: Comparison of numerical and experimental results in terms of position of Body 2 in time and the associated time series of the wave elevations at WP1, WP2 and WP3.

Table 4
Main particulars of the panel meshes used in the computations.

Wave	ω_l (rad/s)	r_{fs} (m)	Free surface panels	Cylinders panels	Total
Reg 1	6.4	3.01	3010	1000	4010
Reg 2	6.8	2.67	2580	1000	3580
Reg 3	7.0	2.52	2324	1000	3324
Reg 4	7.2	2.38	2217	1000	3217

synchronization between numerical and experimental results. The circle markers on the envelope curves indicate the positions of Body 2 for which the WAMIT software was run.

The results show that the hydrodynamic forces and moments F_y, F_z and M_x do not present significant amplitude variations with the change of relative positions between the cylinders. Even though, one may realize that the small modulations observed in the experimental records were very well captured by the TDRPM code. It may also be visualized that the time domain solver provided slightly better results if compared to the software WAMIT, especially for the force F_y as the frequency domain code tends to over-predict the results when Body 2 is located at $x_2 = 0$.

Larger modulations of amplitudes are clearly observed for the hydrodynamic force F_x and moment M_y. As expected, WAMIT provides null values for F_x and M_y when the cylinders are in a tandem configuration in $x_2 = 0$ m. This occurs because its solutions do not include the influence of the wave flow arising from the interaction of the incoming wave with Body 2 in its previous positions. Although in some of these cases the TDRPM and experimental

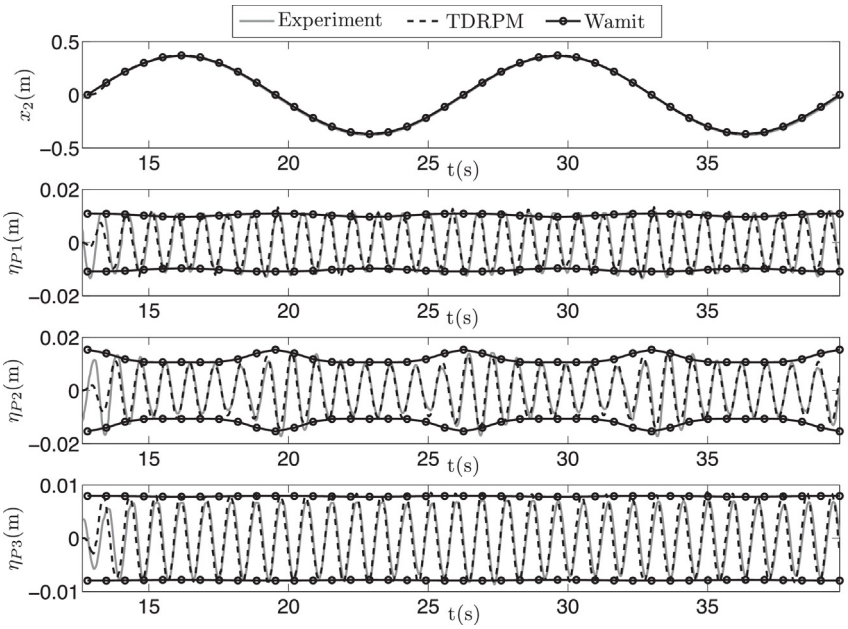

Fig. 34. Case 7: Comparison of numerical and experimental results in terms of position of Body 2 in time and the associated time series of the wave elevations at WP1, WP2 and WP3.

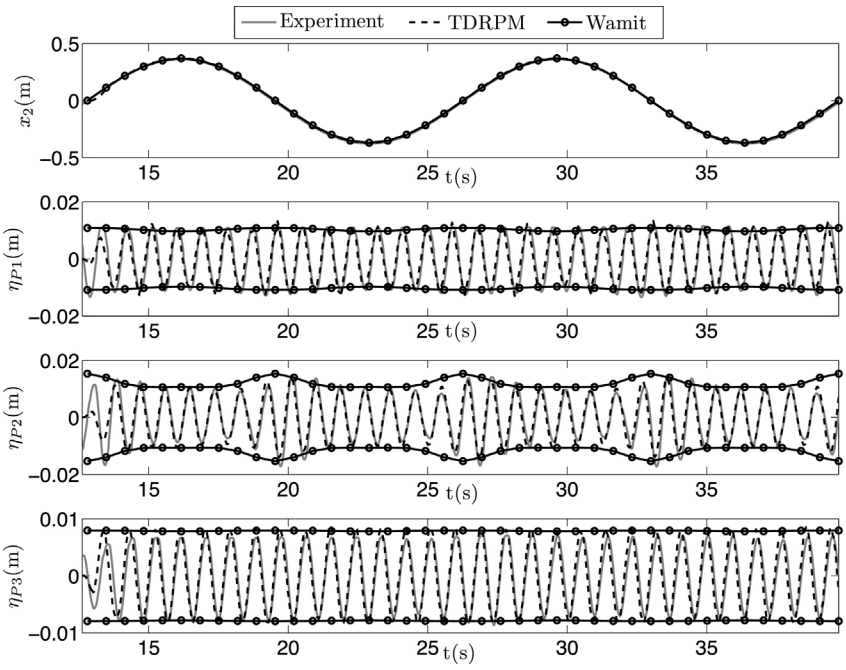

Fig. 35. Case 10: Comparison of numerical and experimental results in terms of position of Body 2 in time and the associated time series of the wave elevations at WP1, WP2 and WP3.

records exhibit small deviations, a overall good agreement is obtained.

An interesting trend is observed in the records F_x and M_y, regarding the fact that the records show that their amplitudes are not the same for "mirror positions". Considering, for instance, the M_y record presented in Fig. 18, one may notice that the hydrodynamic moment M_y is larger when Body 2 is approaching Body 1 in comparison to the situation in which the Body 2 is moving away. Again, this behavior indicates that the flow memory of the wave field, which is not accounted for by frequency domain codes, plays an important role for the proper computation of the hydrodynamic loads, especially when the relative positions of the bodies change relatively fast along the simulations. For example, if one observes the results for Case 3 (Figs. 25 and 26) and Case 5 (Figs. 27 and 28), in which the oscillation frequencies of Body 2 for tests 1 and 4 were reduced to $\omega_{pm} = 6.4/60 = 0.107$ rad/s and $\omega_{pm} = 6.8/30 = 0.2267$ rad/s, respectively, it is possible to realize that the signals become more symmetrical with respect to the mean point of each envelope, presenting approximately the same values for symmetric positions of the bodies with respect to the waves. Furthermore, as these scenarios are now closer to the one assumed by the software WAMIT (since Body 2 moves now more slowly), both numerical methods exhibit a good agreement with the test data.

A better understanding of the non-symmetric pattern is achieved in a simple spectral analysis. Considering again the results for Case 1, Fig. 29 presents comparisons in terms of the energy response spectra for F_x and M_y, from which one may realize that most of the energy is concentrated in two other frequency bands besides the one corresponding to the incident wave frequency (ω_I). This fact reveals that the oscillatory motion of Body 2 induces a Doppler effect in the forces measured on Body 1, which increases or reduces the excitation frequency when Body 2 is approaching or moving away from Body 1, respectively. In fact, since Body 1 is a circular cylinder, the force F_x and moment M_y induced directly by the interaction with the incoming wave tend to vanish, remaining only the force/moment components induced by the waves diffracted from Body 2. Thus, in this problem, Body 2 works as a moving source that emits free surface waves at a constant frequency ω_I. As a result, when Body 2 is approaching Body 1 from negative x coordinates, the wave fronts begin to cluster on the right side of Body 2, while they spread further apart on its left side. This effect modifies the wave frequency perceived by Body 1.

Fig. 29 also indicates that these harmonics correspond to the sum and subtraction of ω_{pm} with the incident wave frequency ω_I. This is also verified by observing the F_x and M_y energy spectra for other cases, such as Cases 2 and 3, in which the oscillatory motion frequencies were reduced to $\omega_{pm} = 6.4/30 = 0.213$ rad/s (Fig. 30) and $\omega_{pm} = 6.4/60 = 0.107$ rad/s (Fig. 31), respectively. Once again, the results provided by the present method recovered very well the experimental data, being able to capture with reasonable accuracy the physics of the problem. A similar behavior was also observed for all the other tests.

Examples of comparisons between numerical and experimental wave elevations for wave probes WP1, WP2 and WP3 (see WPs positions in Figs. 6 and 10) for Cases 1, 4, 7 and 10 are presented in Figs. 32–35. An illustration of the diffraction wave pattern for different instants of the simulation (Case 1) may be observed in Fig. 36. In all these cases the oscillation frequencies of Body 2 were set to $\omega_{pm} = \omega_I/15$ rad/s. One may realize that the wave elevations measured at the WP positioned downstream from Body 1 (WP3 – η_{P3}) present very little variation of amplitude, being almost independent of the translational movement of Body 2. In fact, this wave probe is located at a sheltered area provided by Body 1, where the wave amplitudes are always low.

On the other hand, some amplitude modulations may be observed for WP1 and WP2, for which a very good agreement is again observed between TDRPM computations and experimental records. Indeed, the time domain code presented a slightly better performance if compared to the WAMIT results, predicting the wave elevations in WP2 (η_{P2}) more accurately. As one may observe, for this wave probe the frequency domain results slightly overpredict the wave amplitude when Body 2 is approaching Body 1. Once again, these discrepancies tend to fade away when the period of oscillation of Body 2 is increased, as illustrated by the wave elevations for Cases 3 and 8 displayed in Figs. 37 and 38. In these tests, the

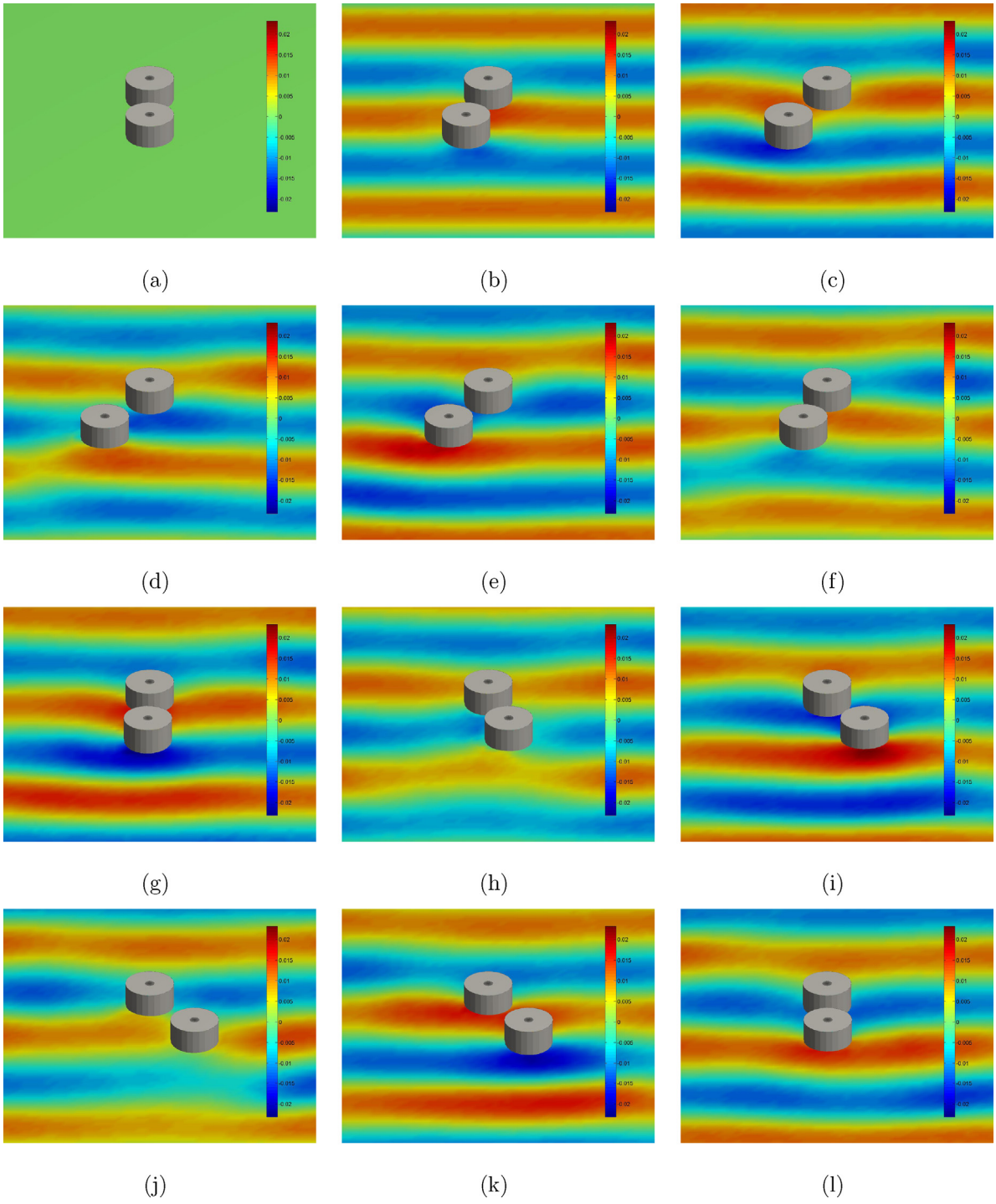

Fig. 36. Case 1: Illustration of the wave pattern for different instants of the simulation.

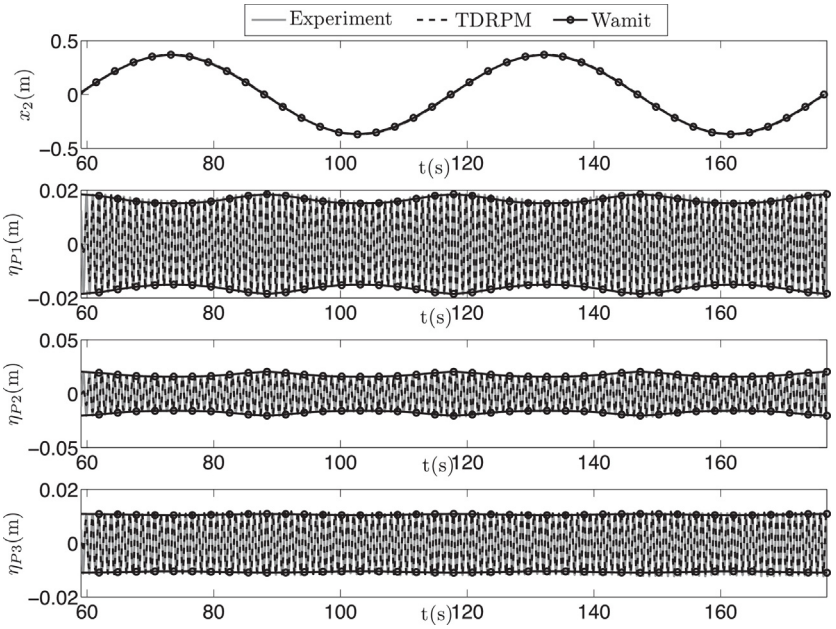

Fig. 37. Case 3: Comparison of numerical and experimental results in terms of position of Body 2 in time and the associated time series of the wave elevations at WP1, WP2 and WP3.

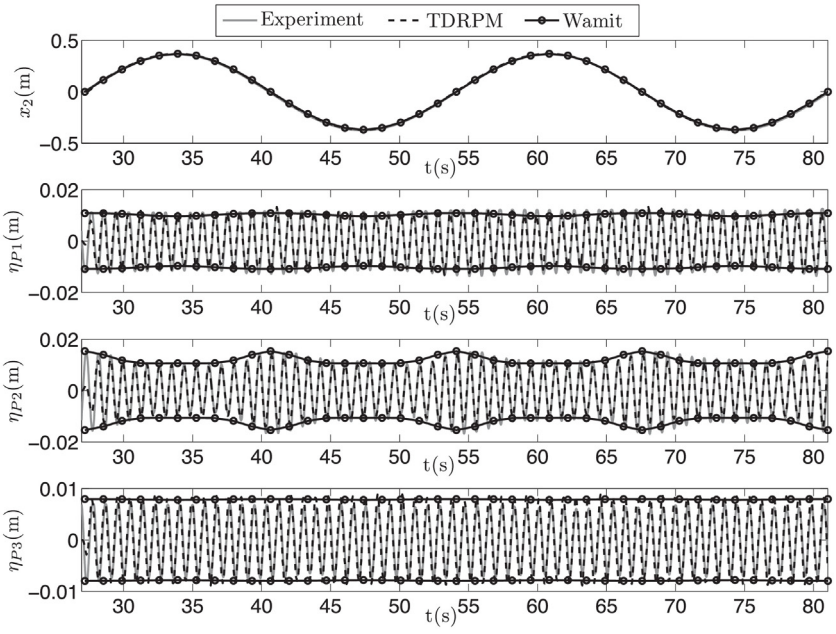

Fig. 38. Case 8: Comparison of numerical and experimental results in terms of position of Body 2 in time and the associated time series of the wave elevations at WP1, WP2 and WP3.

oscillation frequencies were reduced to $\omega_{pm} = 6.0/60 = 0.107$ rad/s and $\omega_{pm} = 7.0/30 = 0.233$ rad/s, respectively.

4. Conclusions

A new method developed to take care of the hydrodynamic interactions on bodies undergoing large relative displacements in waves has been presented, this being a problem that cannot be assessed directly with frequency domain codes. As an important part of this development, a generator of unstructured triangular panel meshes integrated to the time-loop of the code was implemented, so as to account for changes of the relative mean positions of the bodies during the simulations. Moreover, a specific higher order interpolation algorithm had to be used to properly recover the solutions of a previous time-step and to enable the progressing of the calculations with reasonable accuracy.

Benchmark experimental data for assessment of the code performance was obtained through the execution of fundamental captive model tests in a wave basin. The tests considered two captive circular cylinders, being one fixed and attached to a 6 D.O.F. load cell, and the other coupled to a mechanical device that imposed

large and slow horizontal movements of the body. In order to evaluate the influence of the frequency of the prescribed oscillatory motion on the results, three different oscillation frequencies were considered for each regular wave.

Regardless of the fundamental configuration of the tests, the experiments indeed presented a relatively high degree of complexity. Since the main objective was to evaluate the hydrodynamic interaction loads between the bodies, and since these effects are very small in relation to the forces induced by the incident wave itself, special care had to be taken in order to minimize the influence of wave reflections from the tank walls. In fact, this was the main trouble for planning the experimental campaign, because each test case demanded a long period of acquisition, which, by its turn, increased the possibility of wave reflection effects on the results. For this reason, the tests were conducted considering regular waves in a frequency range for which the active wave absorption system available at the CH-TPN basin has its best performance.

The performance of the TDRPM code with the new re-meshing feature was then verified by reproducing the situations tested in the wave basin. Records were directly compared for the hydrodynamic loads measured on the fixed body and also for the wave elevations measured on three different positions (upstream, in between and downstream of the bodies). Comparisons showed that the time series for transversal forces/moments were not symmetric with respect to the mean position, meaning that the forces presented different amplitudes for mirror positions of the bodies. In fact, the analysis showed that symmetry is lost due to the Doppler effect induced by the moving body, a physical behavior that was very well captured by the time domain code.

Furthermore, the results also emphasize the importance of considering the transient solution of the hydrodynamic problem, especially when mean positions of the bodies are expected to change relatively fast, a solution that cannot be obtained in a straightforward manner from the results of a frequency domain analysis. In general, the TDRPM code was able to reproduce the experimental records very well for all cases tested, attesting that the re-meshing algorithm was indeed able to cope with the transient wave effects in the experiments.

Acknowledgements

Rafael A. Watai and Felipe Ruggeri acknowledge FAPESP for the scholarship grants (2010/08778-2) and (2012/06681-7), respectively. Alexandre N. Simos acknowledges his Research Grant by the Brazilian Research Council CNPq. Authors are also thankful to DSc. Pedro Cardoso de Mello for his help during the preparation and execution of the model tests in the TPN wave basin.

References

[1] K. Nishimoto, M.D. Ferreira, M.R. Martins, I.Q. Masetti, P.D. Martins Filho, A.A. Russo, J. Caldo, S.S. Silveira, Numerical offshore tank: development of numerical offshore tank for ultra deep water oil production systems., in: Proceedings of the 22nd International Conference on Offshore Mechanics Artic Engineering, 2003.
[2] E.A. Tannuri, T.T. Bravin, A.N. Simos, K.H. Alves, K. Nishimoto, M.D. Ferreira, Dynamic simulation of offloading operation considering wave interactions between vessels, in: Proceedings of OMAE04 23rd International Conference on Offshore Mechanics and Artic Engineering, 2004.
[3] A. Queiroz Filho, E. Tannuri, DP offloading operation: a numerical evaluation of wave shielding effect, in: 8th Conference on Manouvering and Control Marine Craft (MCMC2009), 2009.
[4] T. Bunnik, A simulation approach for large relative motions of multi-body offshore operations in waves, in: Proceedings of the ASME 2014 33rd International Conference on Ocean, Offshore and Arctic Engineering, OMAE2014, San Francisco, California, USA, 2014.
[5] R.A. Watai, A time-domain boundary elements method for the seakeeping analysis of offshore systems (Ph.D. thesis), University of Sao Paulo, 2015.
[6] R.A. Watai, F. Ruggeri, C.M.P. Sampaio, A.N. Simos, Development of a time domain boundary elements method for numerical analysis of floating-bodies' responses in waves, J. Braz. Soc. Mech. Sci. Eng. (2015).
[7] J.J. Stoker, Water Waves, Interscience Publishers, 1957.
[8] E.F.G. van Daalen, Numerical and theoretical studies of water waves and floating bodies (Ph.D. thesis), University of Twente, 1993.
[9] K. Tanizawa, A nonlinear simulation method of 3-D body motions in waves., in: 10th Workshop on Water Waves and Floating Bodies, Oxford, 1995, pp. 235–239.
[10] M. Israeli, S.A. Orszag, Approximation of radiation boundary conditions, J. Comput. Phys. 41 (1981) 115–135.
[11] H. Prins, Time-domain calculations of drift forces and moments (Ph.D. thesis), Tecnische Universiteit Delft, 1995.
[12] T.H.J. Bunnik, Seakeeping calculations for ships, taking into account the non-linear steady waves (Ph.D. thesis), Technische Universiteit Delft, 1999.
[13] S.Y. Boo, Linear and nonlinear irregular waves and forces in a numerical wave tank, Ocean Eng. 29 (2002) 475–493.
[14] Y.-L. Shao, Numerical potential-flow studies on weakly-nonlinear wave-body interactions with/without small forward speeds (Ph.D. thesis), Norwegian University of Science and Technology, 2010.
[15] L. Zhen, T. Bin, N. De-Zhi, G. Ying, Wave–current interactions with three-dimensional floating bodies, J. Hydrodyn. 22 (2010) 229–240.
[16] R.A. Watai, P. Dinoi, F. Ruggeri, A. Souto-Iglesias, A.N. Simos, Rankine time-domain method with application to side-by-side gap flow modeling, Appl. Ocean Res. 50 (2015) 69–90.
[17] F. Ruggeri, R.A. Watai, A.N. Simos, A higher-order time domain Rankine panel method for linear and weakly non-linear computation., in: ASME 34th International Conference on Offshore Mech. & Artic. Eng. OMAE2015, 2015, St. John's International Conference on Offshore Mech. & Artic. Eng., 2015.
[18] E.A. Tannuri, T.T. Bravin, C.P. Pesce, Dynamic positioning systems: comparison between wave filtering algorithms and their influence on performance, in: ASME 22nd International Conference on Offshore Mech. & Artic. Eng. OMAE2013, 2013, Cancun, Mexico. International Conference on Offshore Mech. & Artic. Eng., 2003.
[19] M.S. Longuet-Higgins, E.D. Cokelet, The deformation of steep surface waves on water: I. A numerical method of computation, Proc. R. Soc. Lond. 350 (1976) 1–26.
[20] R.F. Beck, Y. Cao, T.-H. Lee, Fully nonlinear water wave computations using the desingularized method, in: Proceedings of the Sixth International Conference on Numerical Ship Hydrodynamics, 1994.
[21] P. Ferrant, Simulation of strongly nonlinear wave generation and wave-body interactions using a 3-D MEL model, in: Twenty-First Symposium on Naval Hydrodynamics, 1997.
[22] P.-O. Persson, Mesh generation for implicit geometries (Ph.D. thesis), Massachusetts Institute of Technology, 2005.
[23] Q.X. Wang, Unstructured MEL modelling of nonlinear unsteady ship waves, J. Comput. Phys. 210 (2005) 368–385.
[24] P.C. Mello, M.L. Carneiro, E.A. Tannuri, K. Nishimoto, USP active absorption wave basin: from conception to commissioning, in: Proceedings of the ASME 2010 29th International Conference on Ocean, Offshore and Artic Engineering, OMAE2010, Shanghai, China, 2010.
[25] P.C. Mello, M.L. Carneiro, E.A. Tannuri, F. Kassab Jr., R.P. Marques, J. Adamowski, K. Nishimoto, A control and automation system for wave basins, Mechatronics (2013).